

1 **Wind drift in a homogeneous equilibrium sea**

2 R. M. Samelson

3 *104 CEOAS Admin Bldg, College of Earth, Ocean, and Atmospheric Sciences, Oregon State*
4 *University, Corvallis, OR 97331-5503, USA*

5 *Corresponding author:* R. M. Samelson, roger.samelson@oregonstate.edu

6 ABSTRACT: A simple dynamical model is proposed for the near-surface drift current in a homoge-
7 neous, equilibrium sea. The momentum balance is formulated for a quasi-Eulerian, mass-weighted
8 mean in curvilinear surface-following coordinates. The mean velocities computed by this ap-
9 proach for inviscid Stokes and Pollard waves agree with the corresponding Lagrangian means,
10 consistent with a mean momentum balance that determines mean parcel motion. A semi-analytical
11 log-Ekman model is employed, with a depth-dependent eddy viscosity that depends primarily on
12 two empirical parameters: an ocean surface roughness length z_{0o} , distinct from the atmospheric
13 roughness length z_{0a} in bulk-flux algorithms, and additional wave-correction factor ϕ . Kinematic
14 Stokes drift profiles are computed for two different estimates of quasi-equilibrium sea states and
15 are interpreted as total mean drift profiles to provide semi-empirical calibration references for the
16 model. A third calibration reference, for surface drift only, is provided by the traditional 3%-of-
17 wind rule. For 10-m neutral winds from 3 to 20 m s⁻¹, the empirical z_{0o} ranges from 10⁻³ m to
18 1 m, while ϕ ranges from 0.8 to 0.1. The model profiles show a log-layer structure at the smaller
19 wind speeds and a nearly uniform near-surface shear at the larger wind speeds. The associated
20 dissipation profiles are inversely proportional to depth for the smaller wind speeds and less strongly
21 depth-dependent for larger wind speeds. A small correction to the observed bulk aerodynamic
22 drag coefficient is implied. The model predictions show a basic consistency with several sets of
23 previously published near-surface shear measurements but the comparison is not definitive.

24 **1. Introduction**

25 When the wind blows over the sea surface, the surface of the ocean is set in motion. This motion
26 involves the interaction and coupling of two different fluids, the distortion of the interface between
27 them by spontaneously generated waves with horizontal scales that vary by five or more orders of
28 magnitude, and momentum transport by irregular, nonlinear wave breaking and turbulence. The
29 associated physical problem of understanding and quantifying these various dynamical processes
30 and the resulting mean horizontal near-surface motion has been an object of focused study for over
31 a century and remains an area of active research [see, e.g., Ekman (1905); Taylor (1915); Miles
32 (1957); Phillips (1957, 1977); Rapp and Melville (1990); Xu and Bowen (1994); Anis and Moum
33 (1995); Melville (1996); Banner and Peirson (1998); McWilliams and Restrepo (1999); Greenan
34 et al. (2001); Sullivan and McWilliams (2010); Sutherland and Melville (2015); Pizzo et al. (2016);
35 Grare et al. (2018) and numerous related studies]. The determination of the mean motion – the
36 near-surface wind and wave drift – and its dependence on the wind and wave state is of interest
37 both for intrinsic scientific reasons and because of its practical importance for understanding and
38 predicting the motion of oil spills and other floating materials or objects [see, e.g., Ardhuin et al.
39 (2009); Rascle and Ardhuin (2009); Zelenke et al. (2012); Breivik et al. (2016); Ardhuin et al.
40 (2017); Morey et al. (2018); Rodriguez et al. (2018, 2019); Pizzo et al. (2019); Laxague and Zappa
41 (2020)].

42 The idealized case considered here is that of a homogeneous, equilibrium sea. The most general
43 meaning of homogeneous is implied, so the ocean is taken to have uniform density and neutral
44 stability. The equilibrium condition means, among other things, that the surface wave field is in
45 statistical equilibrium with the wind, so that mean wave amplitudes are independent of time as well
46 as space and there are no horizontal divergences of wave momentum fluxes. Further, there are no
47 temporal or horizontal gradients of any fields – except, of course, the large-scale pressure gradients
48 associated with the geostrophic wind and current – and the only mean divergence of momentum
49 flux is that from the vertical gradient of the vertical flux of horizontal momentum. The form of the
50 associated momentum balance, with Coriolis force balancing vertical stress divergence, is familiar,
51 as this approach either, explicitly or implicitly, has been standard since Ekman (1905). Nonetheless,
52 it has not been clear whether or how wave motions are to be included in this mean momentum
53 balance. This question is especially important for the mean velocity in the near-surface, wave-

54 affected layer. Special attention is therefore paid to the specification of the appropriate averaging
55 procedure.

56 Means are computed with respect to a quasi-Eulerian, mass-weighted average in an orthogonal
57 curvilinear coordinate system relative to the moving sea surface (Section 2.a). The resulting
58 mean momentum balance still takes the familiar classical form, as this form follows from general
59 arguments – essentially the translation invariance of the mean state – that do not require explicit
60 consideration of the time-dependent curvilinear coordinate system (Section 2.b). However, the
61 averaging procedure implies a specific interpretation of the mean horizontal velocity and stress
62 divergence. Further, it is shown analytically that the mean inviscid wave-drift computed by this
63 method agrees with the classical Lagrangian mean – that is, the mean captures the Stokes drift – for
64 both Stokes (1847) and Pollard (1970) waves (Sections 2.c,d). These results are consistent with the
65 assertion that this average yields a mean momentum balance that fully incorporates the total mean
66 parcel motion, including wave effects. For example, if Stokes waves are present in the state over
67 which the mean is taken, the Coriolis force induced by the associated Stokes drift (the so-called
68 “Stokes-Coriolis” terms; e.g., Hasselmann 1970) will be captured in the mean momentum balance.

69 A minimal model for the unknown vertical flux of horizontal momentum in the homogeneous-
70 equilibrium setting is proposed in Section 3. The model resembles a classical mixing-length eddy
71 viscosity but depends on both an ocean surface roughness length z_{0o} – which is distinct from
72 the atmospheric roughness length appearing in bulk-stress algorithms such as that of Edson et al.
73 (2013) – and a novel wave-correction factor ϕ . The wave-correction factor distinguishes it from
74 previous, related models such as those of Madsen (1977), Weber (1983), Bye (1988), Jenkins
75 (1989) and Bourassa (2000). The model can be viewed as a simplified version of the mixing-
76 length eddy-viscosity model explored by Craig and Banner (1994), which was formulated instead
77 for general wind-wave conditions and included an independent evolution equation for a turbulent
78 kinetic energy quantity. The latter is effectively replaced here by the factor ϕ , which along with
79 z_{0o} must be determined empirically as a function of wind speed.

80 An initial attempt is made here to calibrate the wind-speed dependence of these empirical
81 constants by fitting the resulting model velocity profiles to empirical Stokes-drift profiles for
82 wind-dependent equilibrium wave states, supplemented by the 3%-of-wind rule (e.g., Keulegan
83 1951; Van Dorn 1953) for the surface current. The rationale and background for this approach

84 is explained in Section 4. The calibration gives a nominal model of near-surface wind-drift that
85 can be paired with a bulk-stress algorithm such as that of Edson et al. (2013) to provide a nominal
86 wind-dependent description of the near-surface mean flow. It is emphasized that this calibration is
87 necessarily to be regarded as preliminary and tentative, given the indirect method for estimation
88 of the “observed” relation between wind and near-surface currents. A preliminary comparison, in
89 Section 5, of the predicted mean flow from the nominal calibrated model with mean near-surface
90 currents from several existing observational datasets nonetheless shows a basic consistency of the
91 model with the observations.

92 Implicit in the approach is the assumption that the homogeneous, equilibrium state is a useful
93 approximation to typical open ocean conditions. This assumption may be questioned and, in some
94 cases, is clearly violated. On the other hand, essentially the same assumption is made in standard
95 bulk flux parameterizations of air-sea momentum flux (e.g., Garratt 1992; Edson et al. 2013).
96 From this point of view, the present study could be seen as having the goal of extending the near-
97 surface atmospheric wind and stress profiles that are implicit in bulk-stress algorithms through the
98 uppermost few meters of the water column, to obtain matching mean near-surface ocean current
99 and stress profiles that depend in an analogous way upon the 10-m wind.

100 **2. Formulation: mean momentum and wave-drift**

101 *a. Mass-weighted curvilinear-coordinate mean*

102 Consider the problem of averaging beneath a moving interface in a homogeneous, equilibrium
103 sea. Far from the interface, horizontal averaging could be done in standard Cartesian coordinates,
104 after which all horizontal gradients in the resulting averaged momentum equations would vanish
105 except the uniform, constant, large-scale pressure gradient associated with the geostrophic current.
106 For the near-surface problem, however, this averaging would result in a smearing of the interface
107 across a vertical transition zone defined by the amplitude of the free-surface displacements.

108 To preserve the interface in the averaged equations, the averaging may be done instead on surfaces
109 of constant η in time-dependent orthogonal curvilinear coordinates (ξ_1, ξ_2, η) , where $\eta(x, y, t)$ is a
110 pseudo-vertical coordinate with $\eta = 0$ at the interface (Phillips 1977). The corresponding spatial

111 average $\langle \phi \rangle$ of a quantity $\phi(x, y, z, t)$ on the surface $\eta = \eta_0$ may be defined as

$$\begin{aligned} \langle \phi \rangle(\eta_0, t) &= \frac{1}{A_{\eta_0}} \int_{L_z} \int_{L_y} \int_{L_x} \phi(x, y, z, t) \delta(\eta - \eta_0) dx dy dz \\ &= \frac{1}{A_{\eta_0}} \int_{L_{\xi_2}} \int_{L_{\xi_1}} \hat{\phi}(\xi_1, \xi_2, \eta_0, t) J(X, Y, Z)|_{\eta=\eta_0} d\xi_1 d\xi_2 \end{aligned} \quad (1)$$

112 where $\delta(\eta)$ is the Dirac delta distribution, $J(X, Y, Z)$ is the Jacobian of the transformation $(x, y, z) =$
 113 $[X(\xi_1, \xi_2, \eta, t), Y(\xi_1, \xi_2, \eta, t), Z(\xi_1, \xi_2, \eta, t)]$, and the spatial scales L_x and L_y either correspond to
 114 periodicities of the field or are taken suitably large, such that the average converges. In (1),

$$\hat{\phi}(\xi_1, \xi_2, \eta, t) = \phi[X(\xi_1, \xi_2, \eta, t), Y(\xi_1, \xi_2, \eta, t), Z(\xi_1, \xi_2, \eta, t), t] \quad (2)$$

115 is the quantity ϕ written as a function of the curvilinear coordinates, and

$$A_{\eta_0} = \int_{L_z} \int_{L_y} \int_{L_x} 1 \cdot \delta(\eta - \eta_0) dx dy dz = \int_{L_{\xi_2}} \int_{L_{\xi_1}} J(X, Y, Z)|_{\eta=\eta_0} d\xi_1 d\xi_2 \quad (3)$$

116 is defined so that $\langle 1 \rangle = 1$. The transformation to curvilinear coordinates is necessary in order
 117 that the Dirac delta – defined by $\int F(\eta) \delta(\eta) d\eta = F(0)$ for any function F – can be properly
 118 interpreted and the area element $d\xi_1 d\xi_2$ (or $d\xi_1 \wedge d\xi_2$; e.g., Spivak 1965) is properly tangent to
 119 the surface. The mean may be viewed also as the limit of an integral over an infinitesimally thin
 120 volume containing the surface $\eta = \eta_0$.

121 Under the equilibrium assumption, the spatial mean $\langle \phi \rangle(\eta, t)$ from (1) may be further averaged
 122 over time, to obtain the spatio-temporal average $\Phi(\eta)$,

$$\Phi(\eta) = \frac{1}{T} \int_T \langle \phi \rangle(\eta, t) dt, \quad (4)$$

123 where the timescale T either corresponds to a temporal periodicity of the field or is taken suitably
 124 large, so that the average converges. The spatio-temporal average Φ computed by (1)-(4) is a
 125 function only of the pseudo-vertical curvilinear coordinate variable η .

126 For the homogeneous fluid, (1) is a mass-weighted average in (ξ_1, ξ_2, η) -space, with A_{η_0} being
 127 the mass-weighted area (3). Technically, the use of η -surfaces requires that the interface be at least
 128 smooth and single-valued but it is assumed here that the resulting averaged description relative to

129 a well-defined interface is still valid under general conditions, including, for example, the presence
 130 of breaking waves. Even in relatively high sea states, breaking waves cover only a small fraction
 131 of the sea surface, so this assumption is plausibly defensible. Because the average (1) is taken
 132 over space at a fixed time, there is no distinction between Eulerian and Lagrangian means: the
 133 quantity ϕ in (1) may be regarded as either an Eulerian or a Lagrangian property. In Sections
 134 2.c and 2.d, two explicit examples of this averaging are given, for the simpler but related case of
 135 the velocity fields of monochromatic surface gravity waves. In particular, it is shown for these
 136 examples that the mass-weighted curvilinear-coordinate mean (1) recovers the classical Stokes drift
 137 motion, illustrating that this mean captures the total mean horizontal momentum associated with
 138 the total mean parcel motion even in the presence of waves.

139 *b. Mean momentum balance*

140 For the homogeneous equilibrium sea, the only mean divergence of momentum flux in the mean
 141 horizontal momentum equations is that from the vertical gradient of the vertical flux of horizontal
 142 momentum. Denote this mean stress divergence, computed by the mass-weighted mean (1)-(4), by
 143 $S_\tau(\eta)$, and the corresponding means of the horizontal velocity and the Cartesian vertical coordinate
 144 by $\bar{\mathbf{U}}(\eta)$ and $\bar{Z}(\eta)$, respectively. An effective mean stress $\tau(\eta)$ may be defined by integrating S_τ
 145 with respect to \bar{Z} :

$$\tau(\eta) = \tau_0 + \int_{\bar{Z}_0}^{\bar{Z}} S_\tau d\bar{Z} = \tau_0 + \int_0^\eta S_\tau(\eta) \frac{d\bar{Z}}{d\eta} d\eta, \quad (5)$$

146 where τ_0 is the mean wind stress (here taken positive upwards) and $\bar{Z}_0 = \bar{Z}(\eta = 0)$. If the symbol z
 147 is now redefined to denote $\bar{Z}(\eta) - \bar{Z}_0$ rather than the original Cartesian vertical coordinate, then the
 148 corresponding mass-weighted mean horizontal momentum equations have a classical appearance:

$$\rho_o f \mathbf{k} \times \bar{\mathbf{U}}(\eta) = -\mathbf{G}_o - \frac{d\tau}{dz}(\eta). \quad (6)$$

149 In (6), the constants ρ_o and f are the seawater density and the Coriolis parameter, respectively, \mathbf{k}
 150 is the upward unit vector, and \mathbf{G}_o is a constant large-scale pressure gradient. It is assumed that the
 151 horizontal velocity is geostrophic far from the interface,

$$\bar{\mathbf{U}} \rightarrow \bar{\mathbf{U}}_G = \frac{1}{\rho_o f} \mathbf{k} \times \mathbf{G}_o \quad \text{as} \quad z \rightarrow -\infty. \quad (7)$$

152 The deviation of the mean velocity from the geostrophic mean velocity,

$$\mathbf{U} = \bar{\mathbf{U}} - \bar{\mathbf{U}}_G, \quad (8)$$

153 then satisfies

$$\rho_o f \mathbf{k} \times \mathbf{U} = -\frac{d\tau}{dz}. \quad (9)$$

154 It is clear from (9) that, under the assumed homogeneous, equilibrium conditions, the problem
 155 of determining the vertical profile of the mass-weighted mean horizontal velocity – the mean
 156 horizontal momentum – is equivalent to the problem of determining the vertical profile of the
 157 vertical divergence of effective mean stress, $d\tau(\eta)/dz$. Note that the redistribution of momentum
 158 by waves, including breaking waves, is explicitly incorporated into $\tau(\eta)$, as no distinction is made
 159 between wave and turbulent fluctuations.

160 *c. Mean drift: Stokes waves*

161 The main subject of this study is the mean forced velocity response of the near-surface ocean to
 162 steady winds. However, it is useful at this point to derive surface-relative averages of two free-wave
 163 velocity fields, in order (i) to provide explicit analytical examples of the surface-relative averaging
 164 method outlined in Section 2.a and (ii) to obtain the corresponding mean wave-induced velocity
 165 profiles, for later use in Section 4. Results are derived first for classical Stokes waves and then, in
 166 Section 2.d, for Pollard waves.

167 Consider a linear deep-water wave with surface displacement ζ , where

$$\zeta(x, t) = a \cos(kx - \sigma t), \quad (10)$$

168 so that the wave is propagating in the x -direction with phase speed $c_p = \sigma/k = (g/k)^{1/2}$ and has
 169 the associated horizontal velocity field

$$u(x, z, t) = \sigma a e^{kz} \cos(kx - \sigma t), \quad (11)$$

170 which is oriented along the x direction. Here a is wave amplitude, k is wavenumber, σ is wave
 171 frequency, and all variables are dimensional. At a given horizontal point x and time t , it is consistent

172 to consider the expression (11) to be valid for $z \leq \zeta$. Assume further that (10)-(11) are accurate to
 173 second order in the dimensionless wave slope ka , i.e., the errors in (10)-(11) are of order $(ka)^3$
 174 and the wave is a ‘‘Stokes wave.’’

175 The mean (1) may be computed to obtain the mass-weighted mean horizontal surface velocity
 176 for the Stokes wave on surfaces of constant η . At time $t = 0$, or in a frame translating with the wave,
 177 the associated orthogonal curvilinear coordinates are

$$\xi(x, z) = x + a_1 e^{kz} \sin kx + a_2 e^{2kz} \sin 2kx, \quad (12)$$

$$\eta(x, z) = z + a_1 e^{kz} \cos kx + a_2 (1 + e^{2kz} \cos 2kx), \quad (13)$$

178 where

$$a_1 = -[1 - \frac{1}{8}k^2 a^2]a, \quad a_2 = \frac{1}{2}ka^2, \quad (14)$$

179 and the expressions are accurate to second order in wave slope. The transformation (12)-(13) may
 180 be inverted to the same accuracy, giving

$$X(\xi, \eta) = \xi - a_1 e^{k\eta} \sin k\xi + (ka_1^2 - a_2)e^{2k\eta} \sin 2k\xi, \quad (15)$$

$$Z(\xi, \eta) = \eta - a_1 e^{k\eta} \cos k\xi - a_2 + (ka_1^2 - a_2)e^{2k\eta} \cos 2k\xi, \quad (16)$$

181 so that

$$\hat{u}(\xi, \eta) = u(X, Z) = \sigma a \left(e^{k\eta} \cos k\xi - ka_1 e^{2k\eta} \cos 2k\xi \right), \quad (17)$$

182 again to second order in wave slope. To the same order, the mean horizontal velocity on an arbitrary
 183 η surface is then

$$U_s(\eta) = \frac{k}{2\pi} \int_0^{2\pi/k} \hat{u}(\xi; \eta) J(X, Z) d\xi = \sigma ka^2 e^{2k\eta}, \quad (18)$$

184 where to first order in wave slope (Phillips 1977),

$$J(X, Z) = 1 - 2ka_1 e^{k\eta} \cos k\xi, \quad (19)$$

185 so that $A_{\eta_0} = 2\pi/k$. The mean depth $\bar{Z}(\eta) = \langle Z \rangle(\eta)$ of a given η surface is, similarly,

$$\bar{Z}(\eta) = \frac{k}{2\pi} \int_0^{2\pi/k} Z(\xi; \eta) J(X, Z) d\xi = \eta + ka^2 \left(e^{2k\eta} - 1 \right), \quad (20)$$

186 so that $\bar{Z} = \eta$ to first order. The mean horizontal velocity profile as a function of mean depth is
187 therefore

$$U_s(\bar{Z}) = \sigma ka^2 e^{2k\bar{Z}}, \quad (21)$$

188 again accurate to second order in wave slope. The wave-mean horizontal velocity computed by the
189 mass-weighted mean (1) is therefore equal to the classical Lagrangian mean or Stokes drift (e.g.,
190 Phillips 1977). Note that if the Jacobian J in (18) is replaced by $\partial X/\partial \xi$, the resulting mean will
191 be $U_s/2$ (Pollard 1973; Santala and Terray 1992; Smit et al. 2017).

192 *d. Mean drift: Pollard waves*

193 The Stokes wave was derived for a non-rotating fluid and is a consistent first-order dynamical
194 description of linear ocean surface gravity waves at frequencies $\sigma \gg f$. The second-order mean
195 velocity (21) and the classical Lagrangian Stokes-drift parcel motion, however, are constant in time
196 and thus do not satisfy this frequency constraint. This difficulty was recognized by Ursell (1950),
197 who showed that there could be no such mean drift for inviscid waves on a rotating Earth, and
198 later by Hasselmann (1970). Following on this work, Pollard (1970) presented an exact solution
199 of the Lagrangian equations of motion for a surface gravity wave on a rotating Earth, which for
200 frequencies $\sigma \gg f$ agrees with the Stokes wave to first order in the wave slope. In contrast to
201 Stokes waves, however, and consistent with the arguments of Ursell (1950) and Hasselmann (1970),
202 parcel motions in Pollard waves are exactly periodic and exhibit no mean second-order drift.

203 The Pollard solution takes the Lagrangian form $\mathbf{x} = \mathbf{X}^L(\mathbf{x}_0, t)$,

$$X_p(\mathbf{x}_0, t) = x_0 - be^{qz_0} \sin(kx_0 - \sigma t), \quad (22)$$

$$Y_p(\mathbf{x}_0, t) = y_0 + de^{qz_0} \cos(kx_0 - \sigma t), \quad (23)$$

$$Z_p(\mathbf{x}_0, t) = z_0 + ae^{qz_0} \cos(kx_0 - \sigma t), \quad (24)$$

204 where $\mathbf{x}_0 = (x_0, y_0, z_0)$ are the parcel labels and mean parcel positions, the frequency and decay
 205 scale are

$$\sigma = \left(gq - \hat{f}\sigma \frac{q}{k} \right)^{1/2}, \quad q = k \frac{\sigma}{(\sigma^2 - f^2)^{1/2}}, \quad (25)$$

206 and the amplitude constants b and d satisfy

$$b = a \frac{q}{k}, \quad d = a \frac{q}{k} \frac{f}{\sigma}. \quad (26)$$

207 In (25), \hat{f} is the horizontal Coriolis parameter. Pressure P is constant on parcels, $P(\mathbf{x}_0, t) = P(z_0)$,
 208 so the free surface may be defined by $z_0 = 0$.

209 For $\sigma \gg f$, (25) shows that $\sigma = (gk)^{1/2}$ and $q = k$ to leading order in f/σ . The free surface
 210 deformation, (24) with $z_0 = 0$, is then equivalent to (10), and the Lagrangian velocity field is then

$$u_p(\mathbf{x}_0, t) = \frac{\partial X_p}{\partial t} = \sigma a e^{kz_0} \cos(kx_0 - \sigma t), \quad v_p(z_0 = 0) = 0. \quad (27)$$

211 For small amplitude waves, $kx_0 \approx kX_p$ and $kz_0 \approx kZ_p$, and (27) is then likewise equal to (11)
 212 to first order in the wave slope. The Pollard and Stokes waves are therefore indistinguishable at
 213 leading order, for $\sigma \gg f$ and $ka \ll 1$, and the Pollard-wave coordinates (ξ, η) agree with (12)-(13)
 214 to first order in wave slope. However, the velocity fields differ at second order. Averaging the
 215 Pollard-wave velocity on η surfaces over one wavelength gives

$$\begin{aligned} U_p(\eta) &= \frac{k}{2\pi} \int_0^{2\pi/k} u_p[\mathbf{x}_0(\xi; \eta)] J d\xi \\ &= \sigma a \frac{k}{2\pi} \int_0^{2\pi/k} (e^{k\eta} \cos k\xi - 2kae^{2k\eta} \sin^2 k\xi)(1 + 2kae^{k\eta} \cos k\xi) d\xi + \mathcal{O}(k^3 a^3) \\ &= 0 + \mathcal{O}(k^3 a^3). \end{aligned} \quad (28)$$

216 Thus, the second-order wave-mean horizontal velocity $U_p(\eta)$ of the Pollard wave computed by (1)
 217 is zero: there is no wave-induced drift. A similar result is derived by Pollard (1970), showing that,
 218 to leading order, the Eulerian mean of the Pollard wave is equal and opposite to the Stokes mean,
 219 so that the total Lagrangian mean vanishes, as it must for the exactly periodic parcel motions.

220 *e. Mean inviscid wave-drifts*

221 Several points regarding the drift in the two inviscid wave examples are worth noting. First,
222 the quasi-Eulerian mean (1) indeed gives the same mean wave-drift velocity as the classical
223 Lagrangian mean. This, in turn, supports the use of the mass-weighted, surface-following mean
224 (1) in the context of the momentum balance (6), since it captures the total mean parcel motions
225 that must result from the total mean forces exerted. Further, this mean wave-drift velocity can be
226 different for waves that to leading order are indistinguishable from the Stokes wave; in the case of
227 the Pollard wave, for example, the mean wave-drift vanishes.

228 The latter result has been known since Ursell (1950) and Pollard (1970). Although there have
229 been no measurements demonstrating that ocean waves have the linear Stokes wave form to the
230 required accuracy of second order in wave slope, the Stokes-wave Lagrangian drift expression is
231 nonetheless frequently used to estimate surface and near-surface drift velocities under a variety
232 of conditions and for a variety of purposes. In many of these settings, an assumption of quasi-
233 equilibrium for the wave field might be seen as appropriate, which would seem to argue instead for
234 the Pollard-wave model.

235 **3. A wave-modified log-Ekman model**

236 *a. Stress parameterization*

237 The minimal dynamical model of the near-surface, homogeneous-equilibrium wind-drift current
238 proposed here is a generalized log-Ekman model, consisting of the classical quasi-equilibrium
239 momentum balance (9) supplemented by a mixing-length parameterization of the effective turbulent
240 stress τ (29) that depends on two empirical parameters:

$$\tau = -\rho_o A_v \frac{d\mathbf{U}}{dz}, \quad (29)$$

$$A_v(z; U_{10N}) = \phi(U_{10N}) \kappa u_* [z_{0o}(U_{10N}) - z], \quad -z_1 < z < 0. \quad (30)$$

241 The eddy viscosity A_v in (30) depends on an effective ocean roughness length z_{0o} and a wave-
242 correction factor ϕ , both of which are allowed to depend on U_{10N} . Note that the formulation (30)
243 applies only on the ocean side of the interface ($z < 0$) and that the ocean roughness length z_{0o}

244 may, and here generally will, differ from the atmospheric roughness length z_{0a} that appears, for
245 example, in (38).

246 The novel wave-correction factor $\phi(U_{10N})$ is introduced to account for deviations from classical
247 rigid-boundary turbulence that can be expected to arise from surface-wave distortions of the
248 interface and near-surface fluid, including breaking waves and the associated momentum transport.
249 In effect, this factor allows deviations of a wave-modified von Kármán constant $\kappa' = \phi\kappa$ from the
250 classical, rigid-boundary value $\kappa \approx 0.4$. From the point of view of dimensional analysis, surface
251 waves introduce an additional length scale on which the dimensionless shear may depend, allowing
252 departures of κ' from κ . This wave-correction factor is analogous to, but simpler than, the height-
253 dependent stability functions of similarity theory for the atmospheric planetary boundary layer
254 (see, e.g., Sec. 3.3 of Garratt 1992). In the present case, the factor ϕ is a constant (with respect
255 to z , for each value of U_{10N}) rather than a function of stability-scaled height, and from a physical
256 point of view is introduced to represent surface-wave rather than stability effects.

257 The classical form of (30) without the additional parameter ϕ has been previously invoked for
258 the near-surface ocean (see, e.g., Madsen 1977; Jenkins 1989; Lewis and Belcher 2004). The
259 introduction of the novel wave-correction factor ϕ is a modest modification to the classical form
260 but allows a much wider variety of near-surface momentum fluxes and velocity profiles, greatly
261 increasing the potential utility of the resulting modified log-Ekman model, (9) with (29)-(30),
262 as an empirical representation of mean near-surface dynamics. For example, the combination of
263 small ϕ and large z_{0o} can give an eddy viscosity that is large and approximately constant over a
264 finite depth near the surface, potentially consistent with the structure of turbulence injected at the
265 surface by breaking waves (e.g., Agrawal et al. 1992; Thomson 2012; Thomson et al. 2016). A
266 plausible alternative approach could be to represent the wave effects through a separate, wind-
267 speed-dependent body force (e.g., Kudryavtsev et al. 2008).

268 *b. Near-surface structure*

269 It is important to recognize that, although A_v in (30) has a classical law-of-the-wall mixing-
270 length form, solutions of (9) with (29)-(30) will have a constant-stress, log-layer structure near
271 $z = 0$ only for sufficiently small values of z_{0o} . For large values of z_{0o} ($z_{0o} \approx 1$ m, say, for
272 $0.1 < \phi < 1$), the resulting velocity profiles instead more closely approximate the classical Ekman

273 (1905) solutions with a constant eddy viscosity and could, for example, more adequately fit a
 274 locally linear empirical near-surface velocity profile. Such large values of z_{0o} are consistent with
 275 those inferred under breaking surface waves by Craig and Banner (1994), who used a general,
 276 multi-equation, turbulence closure model that is much more complex than (30) but, in the simplest
 277 neutral stability limit, reduces to the classical law-of-the-wall eddy viscosity representation near
 278 the surface, which is (30) with constant z_{0o} and $\phi = 1$. Note this latter, limiting behavior is shared
 279 by a large class of turbulence closure models used in numerical ocean circulation models.

280 Whether a log layer exists near the surface is uncertain and may depend on wind and wave
 281 conditions. Some studies, such as Churchill and Csanady (1983) and Bye (1988) report observations
 282 consistent with a near-surface log layer, a conclusion also reached in subsequent analysis of the same
 283 observations by Bourassa (2000) and supported by the recent, independent observations of Laxague
 284 and Zappa (2020). However, there is no consensus that log-layer behavior is consistently found
 285 in existing measurements of near-surface currents or of near-surface kinetic energy dissipation ϵ
 286 (e.g., Agrawal et al. 1992; Anis and Moum 1995; Thomson 2012; Thomson et al. 2016), where the
 287 latter can be expressed as

$$\epsilon = A_v \left| \frac{d\mathbf{U}}{dz} \right|^2 \quad (31)$$

288 and for a constant-stress log layer with $\phi = 1$ and small z_{0o} should be equal to $u_*^3/[\kappa(z_{0o} - z)] \approx$
 289 $u_*^3/(\kappa|z|)$. It is worth noting that in the atmospheric case, the approximate constant-stress layer
 290 (above a possible wave boundary layer) is often limited by rotation to a height of several tens of
 291 meters; for example, Garratt (1992), Fig. 3.2, p. 46, estimates it as $0.02 D_a$, where $D_a = v_*/f$ and
 292 $v_* < 0.4 \text{ m s}^{-1}$ for $U_{10N} < 10 \text{ m s}^{-1}$ (Fig. 1a). Since the characteristic depth $D_o = u_*/f$ of the ocean
 293 boundary layer is a factor of $\alpha \approx 0.035$ [where α is defined in (A10)] smaller than D_a , this would
 294 suggest that any constant-stress layer on the ocean side would often be limited to a depth of less
 295 than a meter. By this indication, any such constant-stress layer would often be thin relative to the
 296 wave-affected layer and difficult to observe even if it were present. Consequently, it is potentially
 297 important that (30), for large values of z_{0o} , can support solutions without log-layer behavior.

298 *c. Piecewise-linear extension*

299 The solution of (9) with (29)-(30) and $z_1 \rightarrow \infty$ can be obtained in terms of a single modified
 300 Bessel function (Ellison 1956; Madsen 1977; Lewis and Belcher 2004). The simplicity of this

301 solution is appealing but it has the unphysical element that the eddy viscosity increases without
 302 bound away from the sea surface. A model of nearly equivalent simplicity but with a more physical
 303 eddy viscosity profile can be obtained by requiring that the eddy viscosity reach a maximum at the
 304 depth $z = -z_1$, remain constant for $-z_2 < z \leq -z_1$, decrease linearly with depth from its maximum
 305 value to a small value over the interval $-z_3 < z \leq -z_2$, and then maintain that small value for all
 306 depths $z \leq -z_3$. In this case, the equations have solutions in terms of modified Bessel functions in
 307 the subregions $-z_1 < z \leq 0$ and $-z_3 < z \leq -z_2$ and exponential functions (as for the classical Ekman
 308 layer) in the subregions $-z_2 < z \leq -z_1$ and $z \leq -z_3$, with continuity and smoothness conditions
 309 imposed on the velocity at $z = \{-z_1, -z_2, -z_3\}$ (e.g., Samelson et al. 2020).

310 This piecewise-linear extension of (30) for $z < -z_1$ is adopted here, with $\{z_1, z_2, z_3\}$ chosen such
 311 that

$$\phi \kappa u_* (z_{0o} + z_1) = A_{v,max} = 0.03 u_* D_o, \quad (32)$$

$$z_2 = 2 z_1, \quad (33)$$

$$A_{v,max} - \phi \kappa u_* (z_3 - z_2) = A_{v,min} = 0.1 A_{v,max}, \quad (34)$$

312 where the value $A_{v,max} = 0.03 u_* D_o$ was suggested by comparison with large-eddy simulations
 313 similar to those reported by Skillingstad et al. (2017). This modification avoids the unphysical
 314 unbounded growth of A_v with depth but has only a minor effect on the model near-surface velocity
 315 response, because the depth $z_1 \approx 0.1 D_o$ is at least several meters and so beneath the near-surface
 316 regions of large wind-drift shear (see, e.g., Section 3.f).

317 4. Model calibration

318 a. Motivation

319 In Section 2, it was argued that under equilibrium conditions, the near-surface current should be
 320 determined directly by, or from, the mean momentum balance, rather than, for example, through a
 321 separate calculation of a Stokes-wave drift based on an independently specified surface wave field.
 322 It was further demonstrated that surface waves with identical first-order linear dynamics can have
 323 different second-order wave-drift characteristics, raising doubt regarding the meaning of classical
 324 Stokes-drift estimates for quasi-equilibrium seas. However, a number of recent studies have argued

325 that model predictions of surface-drift trajectories have been measurably improved by inclusion of
326 a near-surface velocity derived from wave-field estimates by Stokes-drift calculations. Simulations
327 of Langmuir cell development in the turbulent surface boundary layer are also improved when
328 Stokes-drift estimates of near-surface mean shear are included (e.g., Sullivan and McWilliams
329 2010).

330 These results suggest that the Stokes-drift estimates, even if not well motivated theoretically [as
331 has been recently suggested by Mellor (2016)], provide at least a useful empirical representation
332 of near-surface ocean drift velocities. Motivated by this recognition, wave-drift velocity profiles
333 are computed in Section 4.d for two quasi-equilibrium wave-state formulations. These profiles are
334 then used in Section 4.e to calibrate the proposed model of near-surface drift currents.

335 Under the quasi-equilibrium hypothesis, a unique wave state should be associated with every
336 wind-speed or wind-stress state. Two complementary approaches to deriving approximate, quasi-
337 equilibrium relations between wave state and wind speed are considered. The first (Section 4.b) is
338 based on a recent analysis and calibration of bulk-flux coefficients for air-sea momentum flux, while
339 the second (Section 4.c) depends more directly on wave observations and a classical assumption
340 of fully developed seas. Both of these are chosen for their simplicity; the differences between
341 them may be taken as a measure of the existing uncertainty in any such approximate relations.
342 A classical estimate of the Stokes-wave drift associated with each wave state is then obtained
343 in Section 4.d from a monochromatic theory, with a single wave component. Although more
344 sophisticated estimates based on a spectrum of wave components are possible (Jenkins 1989;
345 Ardhuin et al. 2009; Breivik et al. 2016), the monochromatic theory is adequate for the present
346 purposes, as the two different wave-state relations already provide significantly different wave-drift
347 profiles as functions of U_{10N} , sufficient to illustrate the likely range of uncertainty in the estimates.

348 *b. Bulk-flux wave state*

349 The most comprehensive existing analysis of the dependence of air-sea momentum flux on 10-m
350 winds is that of Edson et al. (2013), the results of which are encapsulated in the COARE 3.5 bulk
351 flux algorithm. In the course of that study, the influence of wave age and wave slope on the relation
352 between 10-m winds and surface stress was examined, with the perhaps surprising conclusion that
353 the wave-state variables added no significant information to the wind-speed dependent formulation.

354 In contrast, for example, significant additional information was found in the measured near-surface
 355 (nominal 10-m depth; see Bigorre et al. 2013) ocean current: replacing the 10-m wind with
 356 the relative wind – the 10-m wind referenced to the near-surface ocean current – was found to
 357 reduce the scatter in the empirical relation between stress and wind. Edson et al. (2013) found a
 358 “simple reason” for the lack of independent information in the wave-state variables: statistically, a
 359 functional relation existed in the data between the wave state and the wind speed. That is, within
 360 the context of existing data sets that constrain the dependence of surface stress on 10-m winds, the
 361 wave state was found to be in effective quasi-equilibrium with the winds.

362 An analytical representation of this implied dependence of wave state on 10-m neutral winds can
 363 be inferred from the results of Edson et al. (2013). A wave-age dependence

$$\frac{v_*}{c_p} \approx 0.03 \times \left(\frac{U_{10N} - 2}{8} \right) \quad \text{for } U_{10N} > 2, \quad U_{10N} \text{ in units of m s}^{-1}, \quad (35)$$

364 is suggested by Figure 9 of Edson et al. (2013), where again v_* is the air friction velocity. Thus,
 365 the wave age has the classical fully-developed-sea value $v_*/c_p \approx 0.03$ for $U_{10N} \approx 10 \text{ m s}^{-1}$, but
 366 otherwise differs from this value (Fig. 1d). Edson et al. (2013) find further that the ratio of the
 367 rough-flow air roughness length z_{0a}^{rough} to the significant wave height H_s is proportional to the
 368 square of the wave age,

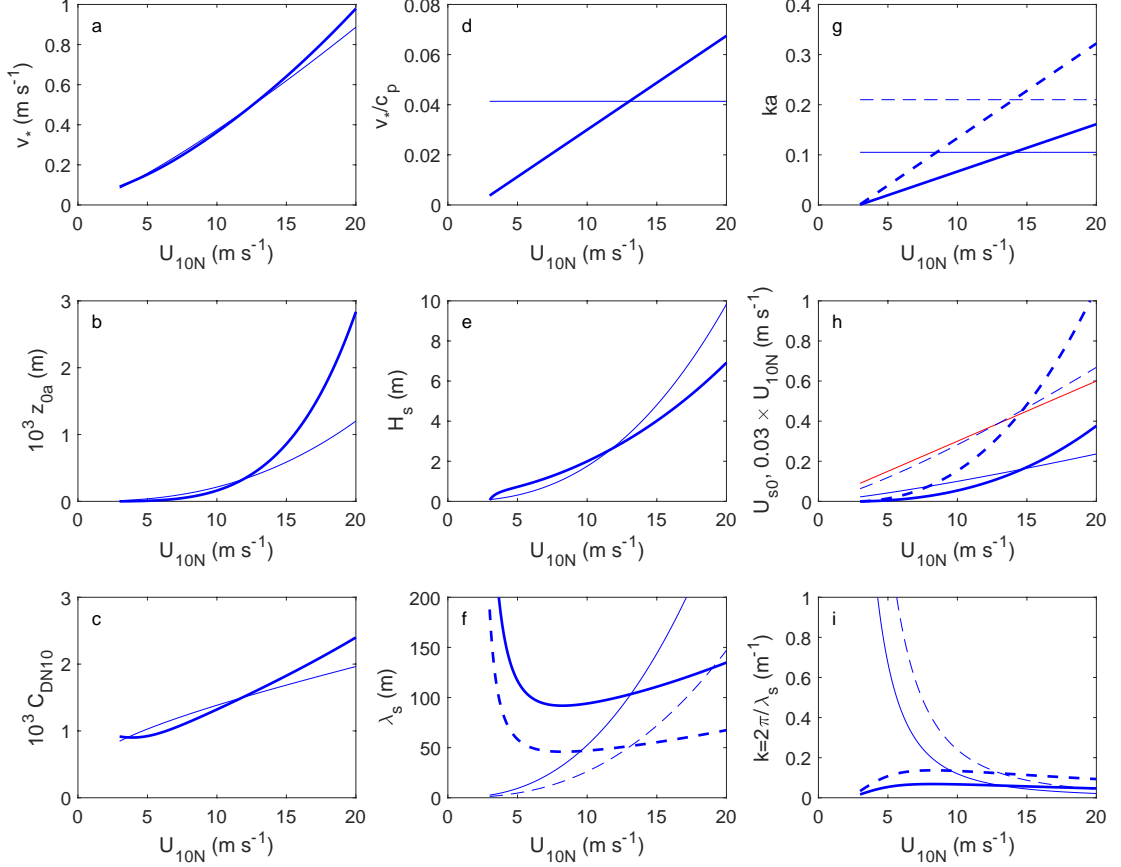
$$\frac{z_{0a}^{\text{rough}}}{H_s} \approx D \left(\frac{v_*}{c_p} \right)^2, \quad (36)$$

369 where the constant value $D = 0.09$ of the proportionality factor gives good agreement, over all sea
 370 states, with the observations on which the COARE 3.5 bulk algorithm is based. Here z_{0a}^{rough} is
 371 defined in terms of the Charnock relation,

$$z_{0a}^{\text{rough}} = \alpha_C \frac{v_*^2}{g}, \quad \alpha_C = mU_{10N} + b, \quad (m, b) = (0.0017, -0.005), \quad (37)$$

372 again for U_{10N} in units of m s^{-1} . Note that z_{0a}^{rough} is related to the COARE 3.5 total roughness
 373 length z_{0a} and neutral drag coefficient C_{DN10} by

$$z_{0a} = \gamma \frac{v_a}{v_*} + z_{0a}^{\text{rough}}, \quad C_{DN10} = \left[\frac{\kappa}{\ln(z_{10}/z_{0a})} \right]^2, \quad (38)$$



376 FIG. 1. Bulk-stress (thick blue lines) and fully-developed-sea (thin blue lines) wave states vs. 10-m neutral
 377 wind U_{10N} : (a) air friction velocity, v_* ; (b) air roughness length $z_{0a} \times 10^3$; (c) 10-m neutral drag coefficient
 378 $C_{DN10} \times 10^3$; (d) wave age v_*/c_p ; (e) significant wave height, H_s ; (f) characteristic wavelength λ_s ; (g) wave
 379 steepness, ka ; (h) surface wave-drift from (21); (i) characteristic wavenumber k . In (f)-(i), the corresponding
 380 values obtained by halving λ are indicated (dashed lines). In (h), the classical 3% rule-of-thumb value for surface
 381 wind-drift is also indicated (red line).

374 where $\gamma = 0.11$, ν_a is the kinematic viscosity of air, $\kappa \approx 0.4$ is the von Kármán constant, and
 375 $z_{10} = 10$ m.

382 With v_* , z_{0a} , and C_{DN10} determined through the COARE 3.5 algorithm for each U_{10N} (Fig. 1a,b,c),
 383 and z_{0a}^{rough} obtained from (38), the significant wave height can be computed from (36) and (35) as

$$H_s(U_{10N}) = \frac{z_{0a}^{\text{rough}}}{D} \left[\frac{8}{0.03 \times (U_{10N} - 2)} \right]^2, \quad U_{10N} > 2 \text{ m s}^{-1}. \quad (39)$$

384 Combining (35)-(37) with the deep-water wave dispersion relation $k = g/c_p^2$ gives the corresponding
 385 characteristic wavelength $\lambda = 2\pi/k$,

$$\lambda(U_{10N}) = 2\pi \frac{D}{\alpha_C} H_s(U_{10N}). \quad (40)$$

386 The resulting significant wave height H_s increases monotonically from zero near $U_{10N} = 3 \text{ m s}^{-1}$
 387 to nearly 7 m for $U_{10N} = 20 \text{ m s}^{-1}$ (Fig. 1e), while the corresponding wavelength λ has a minimum
 388 value of 90 m near $U_{10N} = 7 \text{ m s}^{-1}$ and increases slowly for larger U_{10N} and rapidly for smaller
 389 U_{10N} (Fig. 1f,i).

390 *c. Fully developed seas*

391 An alternative empirical relation between the 10-m wind and wave state can be obtained from
 392 the results of Resio et al. (1999), who proceed under a fully-developed-sea assumption that is
 393 effectively equivalent to assuming a constant value of the wave age,

$$\frac{v_*}{c_p} = \frac{1}{24.18} \approx 0.041, \quad (41)$$

394 and a constant value of the Charnock coefficient,

$$\alpha_C = 0.015. \quad (42)$$

395 The result of their considerations is an empirical expression for the significant wave height H_s in
 396 terms of a wavelength-referenced wind velocity U_r , which is both taken equal to the characteristic
 397 wave phase-speed c_p and empirically related to the 10-m wind:

$$H_s = 0.21 \frac{U_r^2}{g}, \quad U_r = 0.516 \times (U_{10N})^{1.244}, \quad (43)$$

398 again for U_{10N} in units of m s^{-1} . With $U_r = c_p$, the deep-water dispersion relation can be used to
 399 obtain the corresponding wavelength λ , which is then

$$\lambda = \frac{2\pi}{g} U_r^2. \quad (44)$$

400 The relations (41)-(44) also determine v_* , the roughness length $z_{0a} = \alpha_C v_*^2 / g$, and, by the second
 401 equation in (38), the neutral drag coefficient C_{DN10} as functions of U_{10N} , yielding dependencies
 402 of these quantities on U_{10N} that are similar to but weaker than those for the COARE 3.5 algorithm
 403 (Fig. 1a,b,c). The assumed constant wave-age contrasts sharply with the variable wave age inferred
 404 from COARE 3.5 (Fig. 1d) but the resulting significant wave height dependencies on U_{10N} are
 405 nonetheless remarkably similar, differing by more than 1 m only for wind speeds above 15 m
 406 s^{-1} (Fig. 1e). In contrast, the wavelength dependencies on U_{10N} differ substantially except near
 407 $U_{10N} \approx 11 \text{ m s}^{-1}$, with (44) describing a wavelength that increases quadratically with U_{10N} from
 408 near zero at approximately 3 m s^{-1} to over 200 m near $U_{10N} = 16 \text{ m s}^{-1}$ (Fig. 1f).

409 *d. Wave-state Stokes-wave drift*

410 With wave amplitude a taken equal to half of the significant wave (peak-to-trough) height,

$$a(U_{10N}) = \frac{1}{2} H_s(U_{10N}), \quad (45)$$

411 and $H_s(U_{10N})$ and the corresponding characteristic wavelength $\lambda(U_{10N})$ taken either from (39)
 412 and (40) or from (43) and (44), it is straightforward to substitute the wave parameters into (21) to
 413 obtain the mean second-order wave drift for linear Stokes waves. The wave drift is second order
 414 in the wave steepness ka , which depends differently on U_{10N} for the two cases considered: for the
 415 bulk-flux wave state (39) and (40), the steepness increases linearly with U_{10N} , with $ka = \alpha_C / (2D)$
 416 for α_C in (37), while for the fully-developed wave state (43) and (44), the steepness is constant, with
 417 $ka = 0.21/2 = 0.105$ (Fig. 1g). The two steepness estimates are approximately equal for $U_{10N} \approx 14$
 418 m s^{-1} .

419 The resulting monochromatic estimates of the surface wave drift are relatively small, reaching
 420 maximum values of less than 10 cm s^{-1} for $U_{10N} \leq 10 \text{ m s}^{-1}$ (Fig. 1h). These values are considerably
 421 smaller than typical estimates of near-surface Stokes drift, presumably because of the use of
 422 the monochromatic formulation. The present estimates can be made more consistent with the
 423 magnitude of typical estimates by halving the wavelengths λ (Fig. 1f,i) while leaving the amplitudes
 424 a fixed. This has the effect of doubling the steepnesses ka (Fig. 1g) and multiplying the wave-
 425 drift estimates by $2\sqrt{2}$ (Fig. 1h). The resulting, adjusted, surface-drift estimate based on the
 426 bulk-flux wave state (39) and (40) remains less than 0.2 m s^{-1} for $U_{10N} < 10 \text{ m s}^{-1}$ but increases

427 rapidly to more than 1 m s^{-1} at $U_{10N} = 20 \text{ m s}^{-1}$ (Fig. 1h). The adjusted estimate based on the
428 fully-developed-sea wave state (43) and (44), remarkably but presumably accidentally, is nearly
429 indistinguishable from the classical rule of thumb (Keulegan 1951; Van Dorn 1953; Weber 1983;
430 Zelenke et al. 2012; Samelson 2020) according to which the surface drift is 3% of the 10-m wind
431 speed (Fig. 1h). These adjusted estimates and the associated wave-drift profiles can be regarded
432 as anecdotally verified representations of quasi-equilibrium near-surface ocean wind-drift shear.
433 As such, they are used in Section 3 to provide initial, illustrative calibrations of a simple model of
434 near-surface wind-drift shear.

435 *e. Profile fitting*

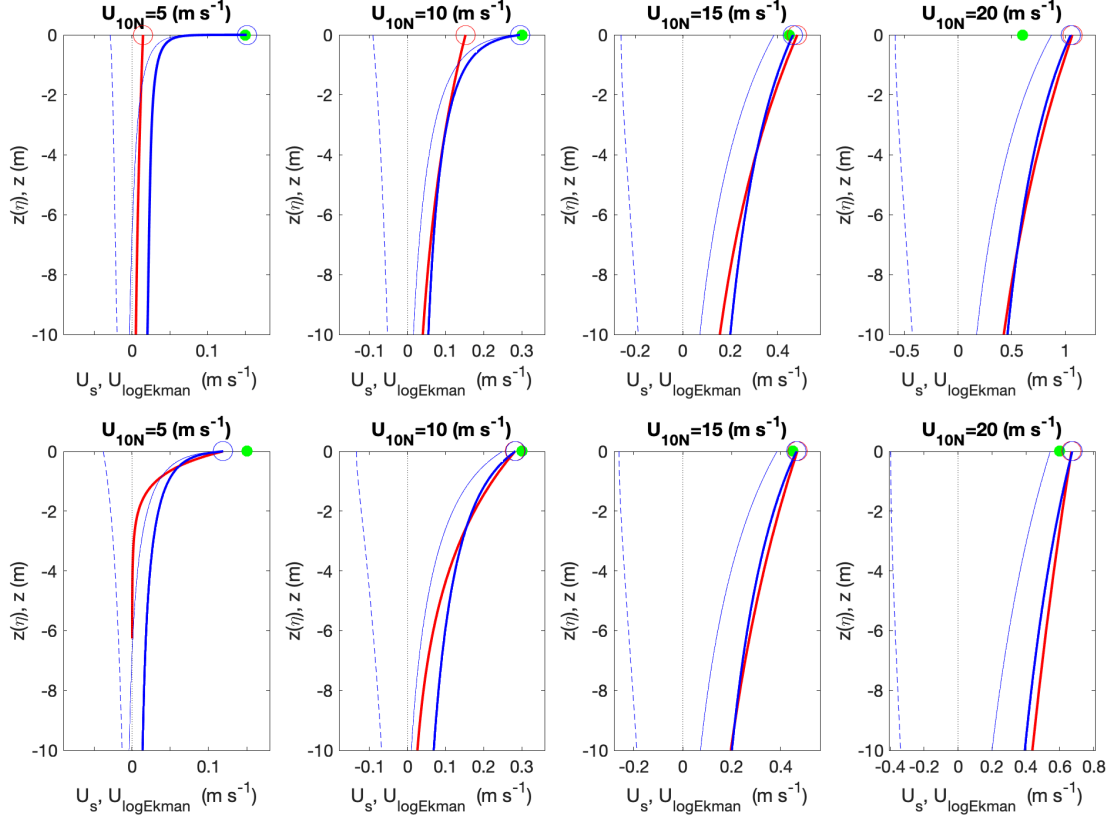
436 The generalized log-Ekman model considered here thus consists of (9) with (30) and the piecewise
437 continuous extension of $A_v(z)$ implied by (32)-(34). This model depends primarily on two empirical
438 parameters, the dimensional effective ocean roughness length z_{0o} and the dimensionless wave-
439 effect factor ϕ . Numerical values for these parameters, as functions of U_{10N} , could in principle
440 be sought by fitting the model velocity profiles to observations, in a manner analogous to the
441 empirical determination of bulk-stress drag coefficients such as that described by Edson et al.
442 (2013). However, a comparably reliable and comprehensive calibration dataset for near-surface
443 currents does not exist, largely because of the inherent measurement challenges in the wave-affected
444 near-surface ocean. Instead, the inferred wave-drift profiles obtained in Section 4 are used here
445 to derive preliminary estimates for the two parameters, as functions of U_{10N} , and to illustrate the
446 range of near-surface velocity profiles that the model can represent.

447 Given the large differences between the two sets of wave-drift profiles and the uncertainty
448 inherent in their representations of ocean near-surface wind-drift, the fitting was done manually
449 by subjective comparison of individual profiles, and for only four values of the 10-m neutral wind
450 speed, $U_{10N} = \{5, 10, 15, 20\} \text{ m s}^{-1}$, with f evaluated at latitude 40°N . The subjective fits generally
451 emphasized the upper portions of the profiles, where the inferred wave-drift velocity and vertical
452 shear are relatively large. For simplicity, the magnitude of the model vector velocity was used
453 for the fit in all cases, so that differences in directionality between the model vector velocity and
454 the unidirectional, nominally downwind wave-drift velocity were neglected, and the relative wind
455 effect was neglected, with stress computed directly from the 10-m wind U_{10N} by the COARE 3.5

456 algorithm of Edson et al. (2013). Alternatively, the downwind component of the model vector
 457 velocity could have been fitted to the wave-drift velocity and the model velocity could have been
 458 used to compute the relative wind, which would have resulted in a different set of fitted parameters
 459 but would not have changed the character of their dependence on U_{10N} . For the bulk-stress wave
 460 state (Section 4.b), the inferred wave drifts for $U_{10N} = \{5, 10\} \text{ m s}^{-1}$ were only a few centimeters per
 461 second, so for those fits the model surface velocity was matched instead to the 3% rule-of-thumb
 462 value, $0.03 \times U_{10N}$, with a transition to the wave-drift profile over the upper meter. Effectively, this
 463 means that the target surface velocity for all the fit cases is the respective maximum of the inferred
 464 wave-drift surface velocity and the 3% rule-of-thumb value.

465 In all cases, the fitted model profiles match the inferred wave-drift profiles within roughly 10%
 466 or, for regions with model velocities below 0.1 m s^{-1} , a few centimeters per second (Fig. 2). A
 467 larger difference occurs immediately adjacent to the surface for the bulk-stress wave state with
 468 $U_{10N} = \{5, 10\} \text{ m s}^{-1}$, because for these cases the model surface velocity was fitted instead to the
 469 3% rule-of-thumb value. For both fitted profiles with $U_{10N} = 5 \text{ m s}^{-1}$, and for the bulk-flux wave-
 470 state fit for $U_{10N} = 10 \text{ m s}^{-1}$, the velocity shear immediately adjacent to the surface is very large, as
 471 the downwind velocity within roughly 0.1 m of the mean sea surface has a classical constant-stress,
 472 log-layer structure, analogous to that below 10-m height in the atmospheric planetary boundary
 473 layer. For the larger wind-speed fits, with $U_{10N} = \{15, 20\} \text{ m s}^{-1}$, the velocity shear is much smaller
 474 near the surface and roughly uniform over the upper 10 m, consistent with the anticipated model
 475 profile structure for large, order 1-m, roughness lengths. The wave-drift profiles for the two cases
 476 with $U_{10N} = 15 \text{ m s}^{-1}$ are very similar, despite partially compensating differences in H_s and λ , and
 477 consequently it was possible to choose a single set of fitting parameters for both of these cases,
 478 giving identical fitted model profiles for these two cases.

485 These fits to the various wave-drift profiles illustrate that the generalized log-Ekman model,
 486 despite depending on only two wind-speed dependent parameters, is able to represent a broad range
 487 of near-surface velocity and shear profiles. This range of velocity and shear profiles corresponds
 488 also to a broad range of profiles of dissipation ϵ , where the latter is computed from (31) for each
 489 profile (Fig. 3). For the weaker wind speeds, $U_{10N} = \{5, 10\} \text{ m s}^{-1}$, the dissipation profiles have
 490 the approximate inverse proportionality to depth that obtains for the constant-stress log layer, with
 491 values between $10^{-5} \text{ m}^2 \text{ s}^{-3}$ near the surface and $10^{-8} \text{ m}^2 \text{ s}^{-3}$ at 10-m depth. For the stronger wind

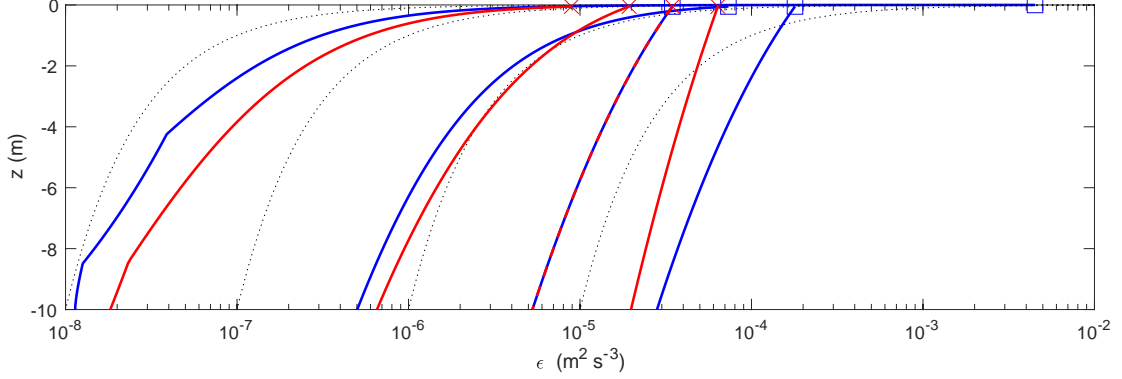


479 FIG. 2. Wave drift (red) and fitted log-Ekman model (blue) velocities (m s⁻¹) vs. depth z (m) for the eight
 480 calibration profiles, for the bulk-flux (upper panels) and fully-developed-sea (lower panels) wave states and for
 481 U_{10N} values as shown. In each panel, the surface values are indicated (red and blue circles) and the $0.03 \times U_{10N}$
 482 rule-of-thumb wind-drift velocity is also shown (green dot). The model velocity magnitude profile (thick) was
 483 used in the fitting. Although not used separately in the fitting, the down-stress (thin) and cross-stress (thin dashed)
 484 vector velocity components from the log-Ekman model are also shown, for completeness.

492 speeds, $U_{10N} = \{15, 20\}$ m s⁻¹, the dissipation is much larger and varies more slowly with depth,
 493 with values between 10^{-4} m² s⁻³ near the surface and 10^{-5} m² s⁻³ at 10-m depth.

500 *f. Fitted parameters*

501 The fitted parameters $z_{0o}(U_{10N})$ and $\phi(U_{10N})$ show consistent dependencies on U_{10N} , with z_{0o}
 502 and ϕ decreasing for increasing U_{10N} (Fig. 4). The inferred z_{0o} values vary by more than 5 orders
 503 of magnitude, from 5×10^{-5} m for the bulk-flux wave state with $U_{10N} = 5$ m s⁻¹ to 12 m for the



494 FIG. 3. Dissipation ϵ ($\text{m}^2 \text{s}^{-3}$) vs. depth z (m) for the bulk-flux (blue) and fully-developed-sea (red) fitted
 495 profiles in Fig. 2. The fit parameters for the two cases with $U_{10N} = 15 \text{ m s}^{-1}$ are the same, so these two profiles are
 496 identical (dashed red-blue). The surface values are indicated for the bulk-flux (blue square) and fully-developed-
 497 sea (red \times) profiles. The largest surface value occurs for the bulk-flux profile for $U_{10N} = 5 \text{ m s}^{-1}$, which has
 498 very large near-surface shear in a classical constant-stress log layer that is fitted to the 3% rule-of-thumb surface
 499 wind-drift velocity.

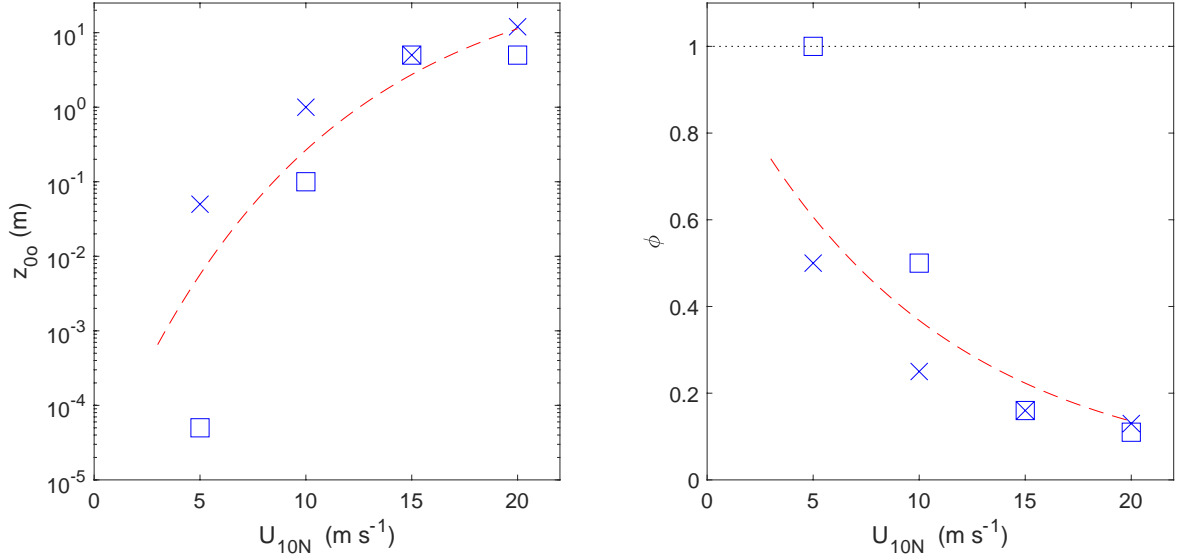
504 fully-developed-sea wave state with $U_{10N} = 20 \text{ m s}^{-1}$. The inferred ϕ values decrease from a
 505 maximum of 1 for the bulk-flux, $U_{10N} = 5 \text{ m s}^{-1}$ wave state to values near 0.1 for both $U_{10N} = 20$
 506 m s^{-1} wave states. There are large differences between the two wave-state parameter fits at each
 507 of the two lower wind speeds, $U_{10N} = \{5, 10\} \text{ m s}^{-1}$. At the $U_{10N} = 15 \text{ m s}^{-1}$, however, the same
 508 values $z_{0o} = 5 \text{ m}$ and $\phi = 0.16$ fit the profiles for both wave states. At $U_{10N} = 20 \text{ m s}^{-1}$, the fitted
 509 values for the two wave-state fits are again similar, though not identical. for (U_{10N}, z_{0o}) in units of
 510 $(\text{m s}^{-1}, \text{m})$.

514 The surface value of the eddy viscosity is proportional to the product of z_{0o} , ϕ , and u_* :

$$A_v(0) = \phi \kappa u_* z_{0o}. \quad (46)$$

515 For the fitted parameters (Fig. 4), this surface value $A_v(0)$ increases by several orders of magnitude
 516 from $U_{10N} = 5 \text{ m s}^{-1}$ to $U_{10N} = 20 \text{ m s}^{-1}$ (Fig. 5a). The near-surface vertical gradient of the eddy
 517 viscosity is proportional to the product of ϕ and u_* ,

$$\frac{dA_v}{dz}(z > -z_1) = \phi \kappa u_*. \quad (47)$$



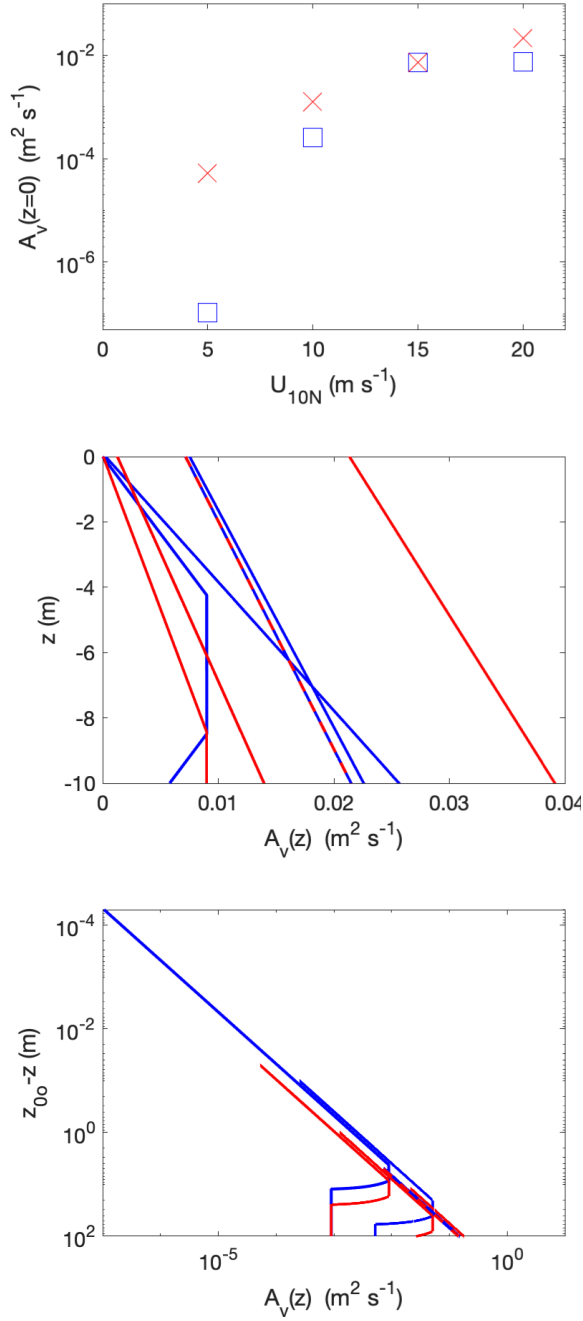
511 FIG. 4. Eddy viscosity parameters z_{0o} (left panel) and ϕ (right) vs. U_{10N} for the eight calibration profiles, for
 512 the bulk-flux (square) and fully-developed-sea (\times) wave states. The approximate empirical relations (48) and
 513 (49) are also shown (dashed red lines).

518 For the bulk-flux wave states, this gradient is weaker for the two larger wind speeds, $U_{10N} = \{15, 20\}$
 519 m s $^{-1}$, and stronger for the two smaller wind speeds, $U_{10N} = \{5, 10\}$ m s $^{-1}$, consistent with the
 520 notion that wave-breaking and other related processes may cause greater homogenization of near-
 521 surface turbulence as wind speeds increase (Fig. 5b). For the fully-developed-sea wave states, this
 522 gradient is essentially independent of wind speed. The depth z_1 is always greater than 4 m, and is
 523 less than 10 m only for the two $U_{10N} = 5$ m s $^{-1}$ fits, and so is beneath the region of large near-surface
 524 shear (Fig. 5b,c).

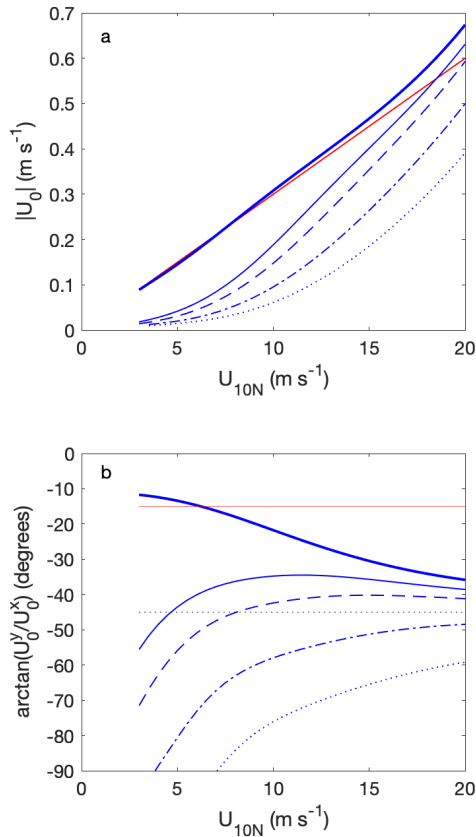
536 The general dependence of the fitted parameters z_{0o} and ϕ on U_{10N} can be characterized by
 537 analytical expressions that nominally interpolate between the fitted values at the four U_{10N} points
 538 (Fig. 4):

$$\log_{10} z_{0o}(U_{10N}) = 2 - 7e^{-0.1U_{10N}}, \quad (48)$$

$$\phi(U_{10N}) = e^{-0.1U_{10N}}, \quad (49)$$



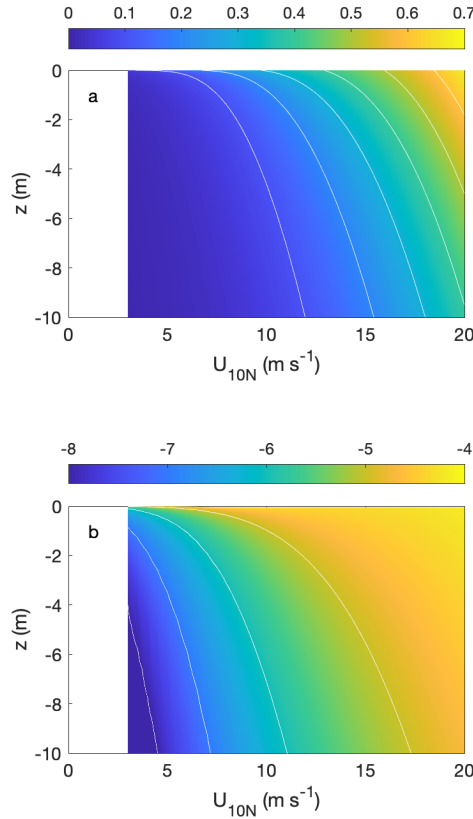
525 FIG. 5. Eddy viscosity $A_v = \phi \kappa u_* (z_{0o} - z)$ for the eight calibration profiles, for the bulk-flux (blue) and fully-
 526 developed-sea (red) wave states: surface value $A_v(0) = \phi \kappa u_* z_{0o}$ (upper panel) and profiles $A_v(z)$ vs. linear
 527 (middle) and logarithmic (lower) depth scales.



528 FIG. 6. Model velocity vs. U_{10N} for the nominal parameterizations (48) and (49), for f evaluated at latitude
 529 40°N . Wind-drift velocity (a) magnitude and (b) angle relative to surface stress, at the surface (thick blue line)
 530 and at depths of 1 m (thin), 2 m (dashed), 5 m (dashed-dotted) and 10 m (dotted), with the 3%, 15° rule-of-thumb
 531 estimate of surface drift (red). In (b), the 45° angle of the classical Ekman-layer surface velocity is also shown
 532 (dotted black).

539 for z_{0o} and U_{10N} in units of m and m s^{-1} , respectively. With this nominal parameterization, model
 540 solutions can be computed over the complete range of U_{10N} values considered, $3 \text{ m s}^{-1} \leq U_{10N} \leq 20$
 541 m s^{-1} . These relations assume, like the model fits above, that f is evaluated at latitude 40°N , but
 542 the results should not depend strongly on this choice provided that equatorial latitudes are avoided.

543 The model solutions for the nominal parameterization (48)-(49) have surface wind-drift velocity
 544 magnitude that is within a few cm s^{-1} of the 3% rule for $U_{10N} < 15 \text{ m s}^{-1}$ and exceeds that estimate
 545 by roughly 10% for larger wind speeds (Fig. 6a). For wind speeds $U_{10N} < 10 \text{ m s}^{-1}$, the direction



533 FIG. 7. Profiles vs. U_{10N} and depth z for model solutions as in Fig. 6. (a) Magnitude of model vector velocity
 534 (m s^{-1} ; shading, white contours at 0.1 m s^{-1} intervals). (b) 10-base logarithm of model dissipation ϵ from
 535 (31), for ϵ in units of $\text{m}^2 \text{ s}^{-3}$ (shading, white contours at unit intervals).

546 of this surface velocity is also within roughly $\pm 5^\circ$ of the 15-degree directional component (“15
 547 degrees to the right of the wind [stress]”) of the 3% rule (Figs. 6b). The shear – in direction (Fig. 6b)
 548 as well as magnitude (Figs. 6a,7a) – is concentrated in the upper 1 m or less for $U_{10N} < 10 \text{ m s}^{-1}$
 549 and becomes progressively more uniform over the upper 5-10 m for $U_{10N} > 10 \text{ m s}^{-1}$. Similarly,
 550 and consistent with the individual fitted profiles (Fig. 3), the model dissipation (31) is concentrated
 551 in the upper 1 m for $U_{10N} < 5 \text{ m s}^{-1}$ and becomes progressively more uniform over the upper 10 m
 552 as U_{10N} increases past 10 m s^{-1} (Fig. 7b). For the larger wind speeds, the surface velocity angle
 553 increases to 35° to the right of the stress, approaching but remaining less than the 45° rotation of
 554 the classical constant- A_v Ekman layer (Fig. 6b).

555 **5. Results**

556 *a. Comparison with near-surface current observations*

557 The nominal calibration (48)-(49) of the log-Ekman model, (9) with (29)-(30) and (32)-(34), was
558 obtained indirectly, by fitting the model velocity profiles to a set of equivalent wave-drift velocity
559 profiles that were taken as representative of near-surface wind drift, as described in Section 3.
560 This indirect approach was taken because a comprehensive dataset of measured mean near-surface
561 currents that would be adequate to provide a direct calibration, analogous to the eddy-covariance
562 flux dataset on which bulk stress algorithms such as that of Edson et al. (2013) are based, is not
563 presently available. It is possible, however, to compare the model predictions with various sets
564 of measurements of near-surface currents that do exist. Three examples of such measurements
565 are considered here, described respectively by Churchill and Csanady (1983); Kudryavtsev et al.
566 (2008), and Morey et al. (2018). Because these measurements were not used in the calibration, the
567 comparisons provide an independent test of the model.

568 Churchill and Csanady (1983) measured near-surface water velocities in Lake Huron and Cape
569 Cod Bay using drifters and drogues whose positions were determined from acoustic travel time
570 and compass-sighting methods. Relative velocity magnitude and direction between 1.2 cm or 2.5
571 cm depths, from surface drifters with 2.4 cm or 5 cm thicknesses, and 1.8 m, from a drifter with
572 drogue 0.3 m in vertical extent centered at 1.8 m depth, were reported as a function of surface wind
573 speed at 3 m height. A total of approximately 24 such measurements were reported (Churchill
574 and Csanady 1983, Table 1). The relative velocity magnitudes were mostly between 0.06 and 0.1
575 m s^{-1} but showed little systematic dependence on wind speed. A difficulty with this comparison,
576 which also arises for the Kudryavtsev et al. (2008) data, is that the observations do not clearly
577 define a systematic empirical relation between wind speed and near-surface currents. Presumably,
578 this is a sampling problem: either the conditions were not close enough to the ideal homogeneous-
579 equilibrium state or the number of measurements were not adequate to reduce the noise from
580 random fluctuations.

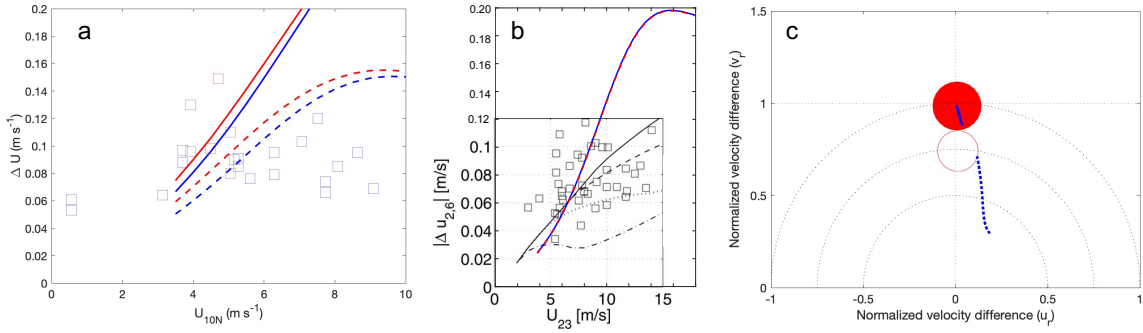
581 The corresponding predicted shear from the log-Ekman model is comparable to the Churchill
582 and Csanady (1983) observations for wind speeds below roughly 7 m s^{-1} but larger than the
583 observations for larger wind speeds (Fig. 8a). For this comparison, observed wind speeds at 3 m

584 height were corrected to nominal 10-m height using a logarithmic profile with constant atmospheric
585 roughness length $z_{0a} = 0.152 \times 10^{-3}$ m; these corrections were of order 10% in observed wind speed
586 and do not affect the basic comparison. Although the model surface current closely follows the
587 3%-of-wind-speed rule, the near-surface shear is so large that the model-predicted shears between
588 1.2 cm or 2.5 cm and 1.8 m depths are significantly below 3% of the wind speed, consistent with
589 the measurements. The model near-surface shear is sufficiently large that the predicted currents at
590 1.2 cm and 2.5 cm differ by a factor of two or more depending on whether they are computed as
591 point values in the vertical or as averages over the 2.4-cm and 5-cm vertical extents of the drifters
592 (Fig. 8a). Larger shears are obtained for the vertical averages, because these contain contributions
593 from the fast, 3%-of-wind surface currents. The point-value estimates show a weaker dependence
594 on wind speed, more consistent with the measurements than the vertical averages.

608 Kudryavtsev et al. (2008) measured near-surface velocities in the Black Sea using drifters with
609 drogues 0.32 m in vertical extent centered at depths between 0.5 m and 5 m, whose positions were
610 determined by laser range-finding. Relative velocity magnitude and direction between drifters at
611 various depths were reported as a function of wind speed measured at 23 m height. The data were
612 not reported numerically, so for this comparison, the model predictions for shear between the 0.5-m
613 and 5-m drifters have been overlaid on a figure from Kudryavtsev et al. (2008), with the model
614 wind speeds at 10 m height corrected to nominal 23-m height, again using a logarithmic profile
615 with constant atmospheric roughness length $z_{0a} = 0.152 \times 10^{-3}$ m. These corrections were again
616 of order 10% in observed wind speed and do not affect the basic comparison.

617 The predictions from the log-Ekman model show a basic consistency with the Kudryavtsev et al.
618 (2008) observations (Fig. 8b). The observed relative velocity magnitudes were between 0.03 and
619 0.12 m s^{-1} and showed little systematic dependence on wind speed. The model predictions are in
620 this same range for wind speeds below 8 m s^{-1} but are two to three times larger for wind speeds
621 above 12 m s^{-1} . With the uppermost profile point at 0.5 m, there is no significant difference
622 between the model predictions obtained from point values and from vertical averages over the
623 drogue extent.

624 Morey et al. (2018) measured near-surface water velocities in the Gulf of Mexico using GPS-
625 tracked surface drifters with 5-cm and 10-cm vertical extent and with a drifter with drogue 0.9
626 m in vertical extent centered at 1 m depth. The observed velocities of the 10-cm and drogued



595 FIG. 8. Comparisons of model predictions with observations from (a) Churchill and Csanady (1983), (b)
 596 Kudryavtsev et al. (2008), and (c) Morey et al. (2018). (a) Observations of 2.5 cm (red squares) and 1.2 cm
 597 (blue squares) to 1.8 m relative velocity magnitude vs. 10-m wind speed, with corresponding model predictions
 598 (red and blue lines, respectively) using vertical averages (solid) or point values (dashed). (b) Observations of
 599 0.5 m to 5 m relative velocity magnitude (squares) vs. 23-m wind speed, with corresponding model predictions
 600 using vertical averages (blue solid line) or point values (red dashed). The additional lines are model fits from
 601 Kudryavtsev et al. (2008). Reprinted with permission from Kudryavtsev et al. (2008), with added overlays.
 602 (c) Observations of 10 cm and 1 m (red solid disk and open circle, respectively, showing approximate extents
 603 of the reported elliptical 95%-confidence intervals about the mean) to 5 cm normalized velocity difference,
 604 with corresponding model predictions (blue solid and dashed lines, respectively). Constant relative velocity
 605 magnitude ratios of 1 (equal magnitudes), 0.75, and 0.5 are indicated (dotted circles centered on the origin, i.e.,
 606 $u_r^2 + v_r^2 = const$). Departures of the u_r value (abscissa) from zero indicate directional differences in the relative
 607 velocity. Adapted from Morey et al. (2018), with added overlays.

627 drifters relative to the 5-cm drifter were reported in terms of distributions of a normalized vector
 628 velocity difference, for which exact equality of a pair of velocities corresponds to the point (0,1) in
 629 the normalized velocity difference plane (their Figure 6, showing normalized velocity differences
 630 defined in their Equation 1). Dependence of the relative velocities on wind speed was not discussed,
 631 so the data are compared here to equivalent normalized vector velocity differences for the full range
 632 of model relative velocities predicted for all values of U_{10N} less than 12 m s⁻¹, the maximum wind
 633 speed reported by Morey et al. (2018) from buoy observations during the observation period (their
 634 Figure 5).

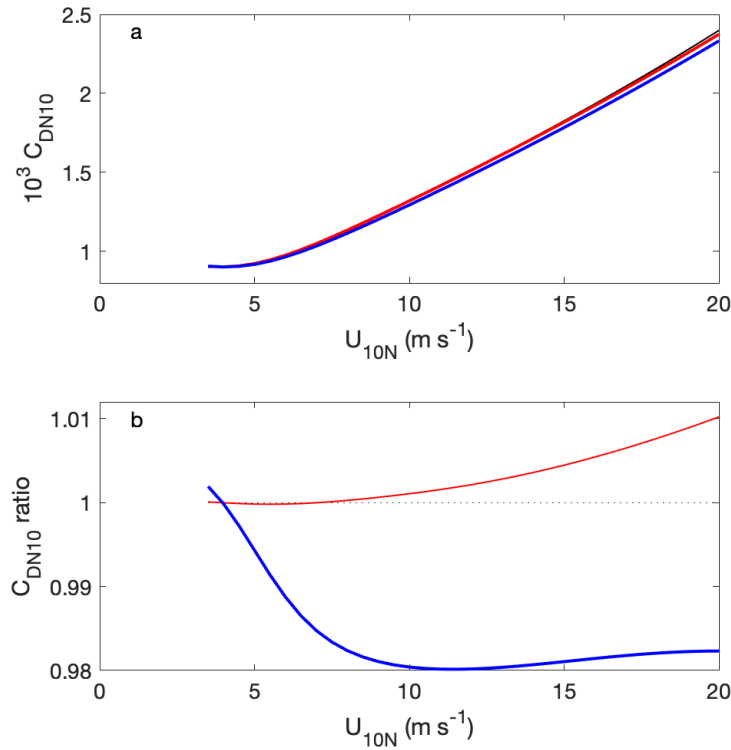
635 Although the wind speed dependence is not addressed in this comparison, the range of predictions
 636 from the log-Ekman model have a basic quantitative similarity to the observations (Fig. 8c). For the

637 relative velocity between 10-cm and 5-cm depths, the model predictions over the full wind-speed
638 range are all within the elliptical 95%-confidence interval about the mean that is reported by Morey
639 et al. (2018). For the relative velocity between the 1-m and 5-cm depths, the model predictions
640 show a normalized relative velocity difference that is roughly twice as large as observed, with a
641 monotonic wind-speed dependence that gives better agreement with the observations at the lowest
642 wind speeds, for which the model values are again within the elliptical 95%-confidence-interval
643 about the mean. With the uppermost profile point at 5 cm, there is again no significant difference
644 between the model predictions obtained from point values and from vertical averages over the
645 drogue extent.

646 *b. Relative wind and drag coefficient*

647 As noted above, the Edson et al. (2013) bulk-stress algorithm should use the relative wind rather
648 than the absolute 10-m wind U_{10N} , where in the calibration with measurements, the ocean surface
649 current is generally taken from observations near 10-m depth. For $U_{10N} > 15 \text{ m s}^{-1}$, the model
650 wind drift velocity at 10-m depth can reach 0.2-0.4 m s^{-1} , comparable to or greater than typical
651 open-ocean mesoscale geostrophic currents. This model wind-drift contribution to the velocity at
652 10-m depth has been neglected in the model calculations of surface stress from U_{10N} , although
653 in principle the equivalent velocity would be included in observational estimates using a relative
654 wind referenced to observed currents at 10-m depth. From this point of view, the drag coefficient
655 used in the model is, effectively, slightly larger than the COARE 3.5 coefficient (Fig. 9).

656 On the other hand, for $U_{10N} < 10 \text{ m s}^{-1}$, the model wind-drift velocity at 10-m depth is negligible
657 but the model wind-drift surface velocity is approximately 3% of U_{10N} , as it is also for $U_{10N} > 10 \text{ m}$
658 s^{-1} (Fig. 6a). If this model surface drift proves to be consistent with observations, the relative wind
659 computed with respect to the wind-drift modified surface current would be reduced by roughly
660 3% at each measured stress. Consequently, a drag coefficient computed for this surface-referenced
661 relative wind would be slightly smaller than the drag coefficient computed for the wind relative to
662 the ocean current at 10-m depth (Fig. 9). In that case, the drag coefficient from the Edson et al.
663 (2013) COARE 3.5 algorithm or any similar formulation would have a small systematic bias if
664 used to compute stress from the exact relative wind, that is, the wind referenced to the current at
665 the ocean surface. This effect, which for the predicted model surface current is approximately 2%



670 FIG. 9. Effective drag coefficient vs. U_{10N} for stress computed from the COARE 3.5 algorithm for relative
 671 wind referenced to ocean currents from the model with nominal parameterizations (48) and (49), for f evaluated
 672 at latitude 40°N . (a) COARE 3.5 $10^3 C_{DN10}$: with no surface-current contribution to the relative wind, as in the
 673 model calculations (black line); with relative wind referenced to the 10-m model current, representative of the
 674 observed relative-wind calibration (red); and with relative wind referenced to the model surface current (thick
 675 blue). (b) Ratios of drag coefficients for no surface-current contribution, as in the model calculations (red), and
 676 for relative wind referenced to the model surface current (blue) to the drag coefficient for relative wind referenced
 677 to the 10-m model current as in the observational calibration.

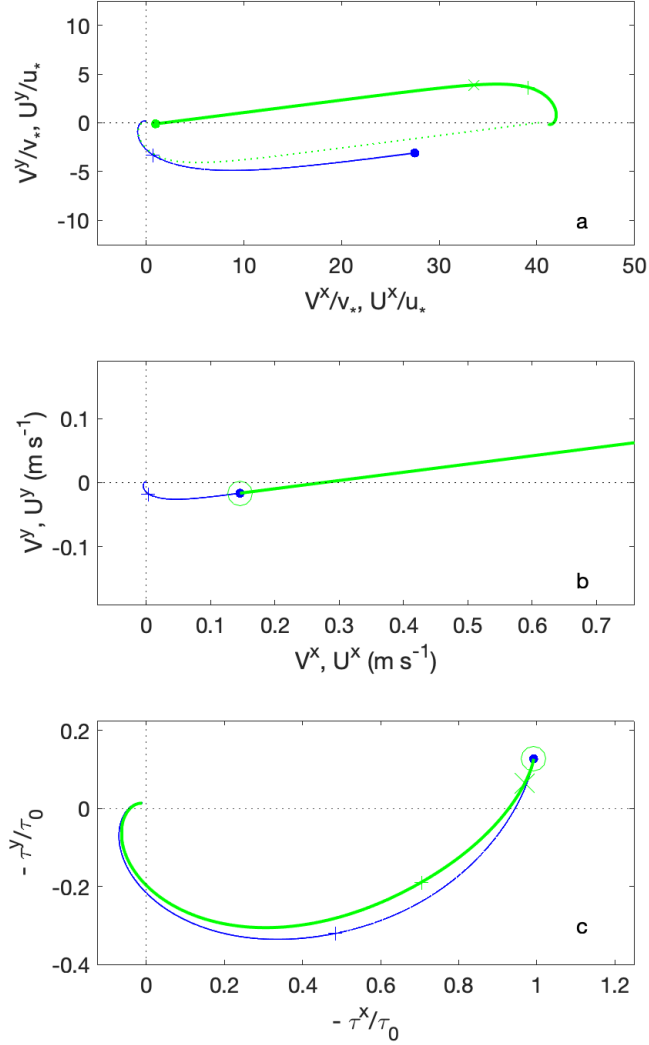
666 for $U_{10N} > 7 \text{ m s}^{-1}$ (Fig. 9b), could be incorporated into the bulk-flux iteration to remove the bias.
 667 The effect is smaller than the 6% that might be inferred as the quadratic effect of a 3% reduction in
 668 relative wind because of the dependence of the COARE 3.5 drag coefficient on U_{10N} , i.e., on the
 669 relative wind.

678 *c. Coupled air-sea boundary layer*

679 The close agreement of the model surface current magnitude with the 3% rule (Fig. 6a) motivates
680 comparison of the coupled ocean-atmosphere boundary-layer profiles with the structure assumed
681 by Samelson (2020), who derived the result (A11) for the interface drift velocity in the case in which
682 there is only a single length scale in each boundary layer. In that case, universality considerations
683 dictate that the dimensionless boundary-layer deviation profiles will be antisymmetric relative to
684 one another, which determines the surface velocity as the weighted mean (A11) of the geostrophic
685 current and wind outside the boundary layer, lending theoretical support to the empirical 3% rule.
686 For this comparison, a form equivalent to (30) was used for the atmospheric eddy viscosity, with
687 an equal dimensionless atmospheric value of z_1 in (32), but with $\phi = 1$ as in classical log-layer
688 theory. For simplicity, the eddy viscosities were held constant at the respective values of $A_{v,max}$
689 for $|z| > z_1$ in both fluids, i.e., the limits $z_2, z_3 \rightarrow \infty$ were taken in (33)-(34).

690 The dimensionless model problem for the coupled boundary layers then consists of (A6) with (30)
691 and (A7), plus their equivalents for the atmosphere, with the continuity conditions for both stress
692 (A8) and velocity (A7) at the mean air-sea interface. The COARE 3.5 drag coefficient (Edson et al.
693 2013) was used to obtain the surface stress from the 10-m wind, again neglecting – for simplicity
694 and consistency with the previous results – any ocean current contribution to the relative wind. The
695 values of z_{0o} and ϕ for the ocean profile are taken from the nominal parameterization (48)-(49).
696 Solutions are found for zero geostrophic ocean current and for a geostrophic atmospheric wind that
697 is directed along the x -axis, with magnitude such that the 10-m wind speed takes a specified value.
698 Note that the 10-wind is then directed roughly 10° to the left of the geostrophic wind rather than
699 along the x -axis, because of the rotation of velocity with height in the boundary layer.

700 The coupled boundary layer solutions for the two 10-m wind values $U_{10N} = \{5, 15\} \text{ m s}^{-1}$ illustrate
701 the differing character of the response at low and at high wind speeds. For $U_{10N} = 5 \text{ m s}^{-1}$, the
702 dimensionless ocean velocity is approximately an antisymmetric reflection of the atmospheric
703 profile (Fig. 10a). The primary asymmetry arises from the truncation of the profile at the ocean
704 roughness length $z_{0o} \approx 5 \times 10^{-3} \text{ m}$, which, from a dimensionless perspective, is substantially
705 larger than the atmospheric roughness, i.e., $z_{0o} \gg \alpha z_{0a}$ for the COARE 3.5 z_{0a} from (38). This
706 leads to a small clockwise rotation of the surface velocity past the geostrophic wind direction
707 (Fig. 10b). The dimensional stress profiles for this coupled boundary layer solution are likewise



710 FIG. 10. Hodographs of ocean (blue) and atmosphere (green) model profiles of (a) dimensionless and (b)
 711 dimensional velocity, and (c) dimensionless downward stress, for the coupled boundary layer solution with
 712 $U_{10N} = 5 \text{ m s}^{-1}$. The levels $z_1^{\{o,a\}} \approx 0.1\{u_*, v_*\}/f$ (+) and the 10-m height in the atmosphere (x) are marked. In
 713 (a), the antisymmetric reflection of the atmospheric profile is indicated (green dotted line).

708 nearly symmetric (Fig. 10c). For these small wind speeds and small values of z_{0o} , the model
 709 response thus approximately exhibits the universality invoked by Samelson (2020).

714 For $U_{10N} = 15 \text{ m s}^{-1}$, the dimensionless ocean velocity departs substantially from the antisym-
715 metric reflection of the atmospheric profile, with a much larger deflection of the surface velocity
716 past the geostrophic wind direction (Fig. 11a,b). One source of the asymmetry is the essentially
717 complete removal of the constant-stress log layer in the ocean through the truncation of the profile
718 at the ocean roughness length $z_{0o} \approx 2.7 \text{ m}$, a value that is several orders of magnitude larger than
719 the atmospheric roughness length and is larger than the thickness of the ocean log layer that would
720 obtain if z_{0o} were comparable to z_{0a} . An additional source of asymmetry is the increased clockwise
721 rotation of the surface velocity past the geostrophic wind direction (Fig. 11b). The dimensional
722 stress profiles for this coupled boundary layer solution remain approximately symmetric but are
723 distorted in relative dimensionless height, as can be inferred from the positions on the hodograph
724 of the respective z_1 points (Fig. 10c). Thus, while the model surface velocity magnitude for
725 $U_{10N} = 15 \text{ m s}^{-1}$ remains close to the 3% rule, the corresponding profiles depart significantly from
726 the antisymmetry that would be implied by the turbulent universality argument of Samelson (2020).
727 These departures arise as asymmetries induced by the the nominal parameterization (48)-(49) for
728 the ocean roughness length and wave correction factor, which result in a dimensionless ocean eddy
729 viscosity profile that differs significantly from its atmospheric counterpart.

730 *d. Wind drift and wave drift*

731 In many theoretical modeling studies of near-surface shear, the wave and locally wind-driven
732 motions are treated separately. In this “wave-kinematic” approach, a mean drift motion is inferred
733 from the wave state using the theory of Stokes (1847) and its modern extensions (e.g., Phillips 1977;
734 Bye 1988; Jenkins 1989; McWilliams et al. 1997; Ardhuin et al. 2009; Breivik et al. 2016; Suzuki
735 and Fox-Kemper 2016). The wave state may be imposed arbitrarily or it may be derived from an
736 independent dynamical model of the wave field. Several important assumptions, often unstated,
737 are implicit in this approach, including: the waves are Stokes waves and as such are linear to second
738 order in wave slope, as is required for the consistency of the second-order Stokes drift calculation;
739 the wave momentum and energy balances are independent of the mean-drift momentum and energy
740 balances to an equivalent order; the mean water parcel motions can be decomposed unambiguously
741 into components driven by the wave field (“Stokes drift”) and by the wind (“wind drift”), again to
742 an equivalent order.

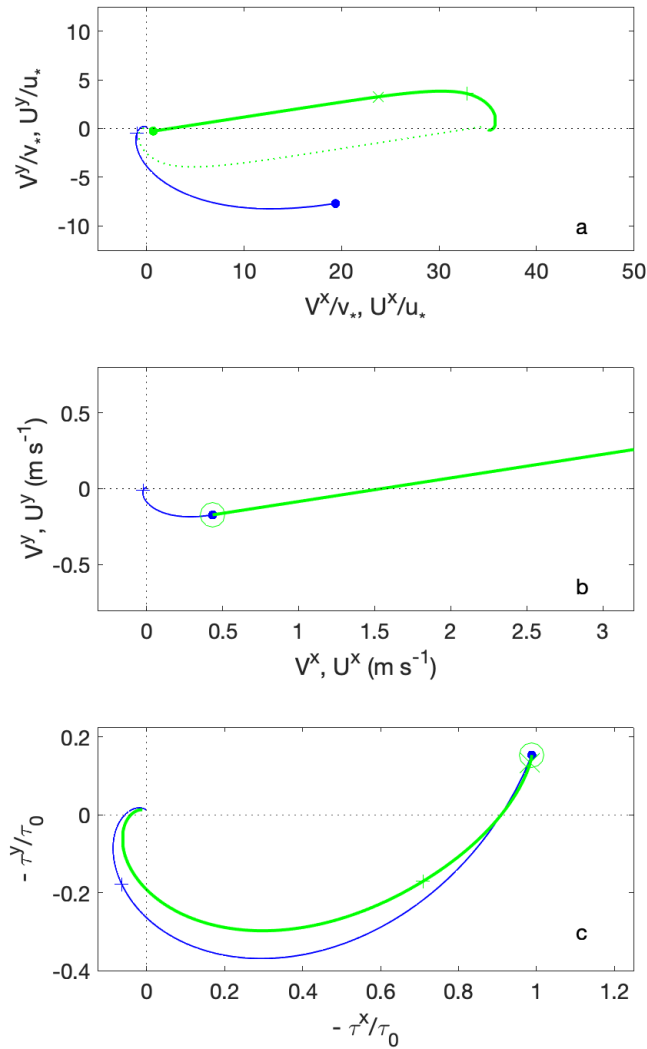


FIG. 11. As in Fig. 10 but for the solution with $U_{10N} = 15 \text{ m s}^{-1}$.

743 For typical conditions in the open ocean, the implicit assumptions of the wave-kinematic approach
 744 are arguably open to doubt. Breaking waves are often observed, even under light winds, calling into
 745 question the assumed linearity to second order required for the Stokes theory to hold rigorously.
 746 Near-surface turbulence is likewise broadly observed and intrinsically nonlinear, potentially incon-
 747 sistent with both the assumed independence of momentum and energy balances and the associated
 748 decomposition of parcel motions. Further, Ursell (1950) has shown that in the presence of the

749 Earth's rotation, a mean Stokes drift cannot be sustained by isolated wave motions. This result was
750 illustrated by the Pollard (1970) exact nonlinear solution for surface waves with rotation discussed
751 in Section 2.d, which (in the high-frequency, small slope limit) is identical to the Stokes wave at
752 linear order but has a second order component that precisely cancels the mean Lagrangian motion
753 that would otherwise be inferred from a Stokes-drift calculation. No measurements of open-ocean
754 surface waves exist that have sufficient accuracy to distinguish between Pollard and Stokes waves,
755 but theory would seem to favor Pollard, given that the importance of the Earth's rotation for mean
756 open-ocean motions is generally well established. For the wave-kinematic framework, extensions
757 of the Ursell (1950) result that attempt to address this difficulty by introducing a wave-derived
758 mean Coriolis force in the mean momentum balance have been developed by Hasselmann (1970)
759 and others.

760 The alternative approach taken here does not suffer from these potential deficiencies but relies
761 instead on the assumption of an idealized homogeneous, equilibrium sea state. Under these
762 conditions, it is appropriate to develop a single description for the total mean drift, including the
763 mean over all wave and wave-related motions. The mass-weighted curvilinear coordinate mean
764 (1) is the appropriate average on which to base this description. In this homogeneous-equilibrium
765 setting, the surface-wave dynamics that may drive Stokes drift and therefore also any Stokes-drift
766 motions that may occur, are indistinguishable in the mean momentum balance from the rest of the
767 wave-turbulent shear flow dynamics that contribute to the mean flux divergence. Consequently, the
768 equilibrium surface and near-surface velocity response can and should be characterized generally
769 as a wind drift, because all the motions, including those that might invite interpretation as waves or
770 wave-related, are driven and maintained by the wind. There is therefore neither need nor advantage
771 in this setting to enforce a separation of wave and other motions. All that matters is the mean
772 vertical flux of horizontal momentum.

773 **6. Summary**

774 A nominal model has been proposed here for the near-surface ocean wind-drift under homo-
775 geneous, equilibrium conditions. The model consists of the mean momentum balance (9) with
776 the mixing-length eddy viscosity (29)-(34) and the empirical parameterizations (48)-(49) for the
777 ocean surface roughness length z_{0o} and wave correction factor ϕ as a function of 10-m wind speed.

778 The mean momentum balance is formulated in terms of a mass-weighted average (1) in surface-
779 following, orthogonal curvilinear coordinates, which captures the total mean parcel motion that
780 must respond the mean forces. This model is envisioned as a continuation into the near-surface
781 ocean of the model atmospheric boundary-layer wind profile that is implicit in bulk-stress algo-
782 rithms such as that of Edson et al. (2013). In the absence of an adequate observational dataset
783 describing near-surface currents as a function of 10-m wind, the calibration (48)-(49) was based on
784 the assumption that computed Stokes-drift velocities provide a first-order estimate of the wind drift
785 in the homogeneous, equilibrium setting. The calibration was conducted for a Coriolis parameter
786 evaluated at 40° N and in general may have a latitude dependence that has not been explored here.

787 For 10-m neutral winds varying between 3 and 20 m s^{-1} , the inferred z_{0o} ranges from 10^{-3} m to
788 1 m, while ϕ ranges from 0.8 to 0.1. The largest values of z_{0o} are comparable to the value inferred
789 by Craig and Banner (1994) in a closely related study that used a more complex turbulence closure
790 formulation with an independently predicted turbulent kinetic energy variable. The model profiles
791 show a log-layer structure at the smaller wind speeds and a nearly uniform near-surface shear at
792 the larger wind speeds. The associated dissipation profiles are inversely proportional to depth for
793 the smaller wind speeds and less strongly depth-dependent for larger wind speeds. The nominal
794 model ocean surface velocity magnitude closely follows the classical 3%-of-wind-speed rule of
795 thumb but, for 10-m winds greater than 10 m s^{-1} , shows a greater rotation away from the wind
796 direction than the 15° suggested by the rule.

797 The model predictions of near-surface wind-drift shear show a basic consistency with the obser-
798 vations described by Churchill and Csanady (1983); Kudryavtsev et al. (2008), and Morey et al.
799 (2018) but the comparison is not definitive. A small correction to the observed bulk aerodynamic
800 drag coefficient is implied by this nominal model, when the relative wind is computed with respect
801 to the ocean current at the sea surface rather than at 10-m depth. Because the wind-drift model
802 parameters are determined by the 10-m wind, the correction could be incorporated directly into
803 the drag coefficient. For observations, where measurements of currents above 10-m depth are
804 difficult and remain rare, this correction may in general not be required. For numerical models
805 with sufficiently fine vertical resolution near the ocean surface, however, it may be more generally
806 appropriate (e.g., Samelson et al. 2021).

807 The nominal calibration (48)-(49) of the model has been obtained here in an indirect manner.
808 Comparisons with existing observations are encouraging but the model will remain preliminary
809 until a reliable calibration dataset for near-surface ocean currents as a function of wind speed,
810 similar to the eddy covariance datasets for air-sea momentum exchange, is available. Recent,
811 renewed attention to measurement of near-surface currents and an associated new generation of
812 remote sensing and in-situ instruments (Ardhuin et al. 2017; Callies et al. 2017; Lund et al. 2018;
813 Morey et al. 2018; Rodriguez et al. 2018, 2019; Hughes et al. 2020; Laxague and Zappa 2020;
814 Grare et al. 2021; Lenain and Pizzo 2021), supplemented by novel analysis approaches, promise a
815 rich set of new observations relevant to this problem in the near future. It is hoped that the present
816 model will provide a useful framework for comparison and analysis of these new observations.

817 *Acknowledgments.* This research was supported by the National Aeronautics and Space Ad-
 818 ministration (NASA) Ocean Vector Winds Science Team (NASA Grant Nos. NNX14AM66G
 819 and 80NSSC19K0061) and the NASA Earth Venture Suborbital-3 program (NASA Grant No.
 820 80NSSC19K1011).

821 *Data availability statement.* No datasets were generated and only previously published datasets
 822 were analyzed during the current study.

823 APPENDIX

824 **Boundary conditions and dimensionless formulation**

825 If the stress τ is taken to depend on the mean flow \mathbf{U} by relations such as (29)-(30), then (9)
 826 can be regarded as a differential equation, the solution of which is the desired velocity profile. In
 827 the classical theory of Ekman (1905), for example, the stress is taken proportional to the mean
 828 shear and the solution can be obtained in terms of complex exponentials. In general, to solve the
 829 resulting differential equation, boundary conditions are needed. The assumption (7) implies that
 830 the velocity deviation \mathbf{U} vanishes far from the interface:

$$\mathbf{U} \rightarrow 0 \quad \text{as} \quad z \rightarrow -\infty, \quad (\text{A1})$$

831 which provides one of the needed boundary conditions.

832 The averaging with respect to surfaces of constant η in each fluid is assumed to preserve the
 833 standard conditions of continuity of velocity and stress at the interface of two viscous fluids
 834 (Batchelor 1967). These conditions are therefore taken to hold for the mean velocities and stress
 835 at the mean air-sea interface $z = 0$:

$$\bar{\mathbf{U}} = \bar{\mathbf{V}} \quad \text{at} \quad z = 0, \quad (\text{A2})$$

836 or, equivalently,

$$\mathbf{U}(z = 0) - \mathbf{V}(z = 0) = -(\bar{\mathbf{U}}_G - \bar{\mathbf{V}}_G) \quad \text{at} \quad z = 0, \quad (\text{A3})$$

837 and

$$\tau(z \rightarrow 0^+) = \tau(z \rightarrow 0^-) = \tau_0. \quad (\text{A4})$$

838 In (A4), τ_0 is the mean stress at the interface, with $z \rightarrow 0^+$ and $z \rightarrow 0^-$ denoting the limits as
839 the interface $z = 0$ is approached from above and below, respectively. In the continuity condition
840 (A2) or (A3) for velocity, $\bar{\mathbf{V}}$, $\bar{\mathbf{V}}_G$ and \mathbf{V} are the atmospheric mean, geostrophic, and boundary-layer
841 deviation (ageostrophic) velocities, analogous to $\bar{\mathbf{U}}$, $\bar{\mathbf{U}}_G$ and \mathbf{U} . The continuity at the interface
842 holds also for the mean pressure.

843 The averaged stress τ_0 incorporates both the viscous stress at the interface and the momentum
844 flux from correlations of pressure and interface slope fluctuations, such as those associated with
845 wind-driven wave fields. As no distinction is made between wave and turbulent fluctuations,
846 no assumption need be made regarding the relative contributions of the pressure and viscous
847 components to the total momentum flux τ_0 across the interface. The vertical integral of (9) gives
848 the classical Ekman transport relation (Ekman 1905),

$$\mathbf{T}_E = \int_{-\infty}^0 \mathbf{U} dz = \frac{1}{\rho_0 f} \mathbf{k} \times \tau_0 = -\frac{1}{\rho_0 f} \mathbf{k} \times \tau^w, \quad (\text{A5})$$

849 which shows that the depth-integrated horizontal boundary-layer transport \mathbf{T}_E is directed to the
850 right of the downward wind stress $\tau^w = -\tau_0$ for $f > 0$, and is independent of any assumption
851 regarding the relation between the mean stress and mean shear.

852 When the mean stress is taken proportional to the mean shear, the resulting vector differential
853 equation (9) is second order in each component, regardless of whether the proportionality factor
854 is constant or depends on z , and only two vector boundary conditions are in general required.
855 Typically, the two boundary conditions (A4) and (A1) are imposed, and the third condition (A2)
856 is treated as a prediction of the surface wind drift in response to the imposed stress (e.g., Ekman
857 1905; Madsen 1977; Weber 1983). This approach is taken for most of the ocean boundary layer
858 model solutions considered here (Sections 4 and 5.a).

859 A similar approach to that outlined in Section 2.b can be taken to obtain mean momentum
860 equations for the atmospheric flow above the sea surface, under similar homogeneous, equilibrium
861 conditions. It is natural then to solve the resulting differential equations simultaneously in both
862 boundary layers and to impose the continuity conditions for both stress (A4) and velocity (A3) at
863 the interface (e.g., Samelson 2020). This approach is taken for the illustrative coupled boundary
864 layer model solutions in Section 5.c.

865 The fundamental velocity and time scales, $u_* = |\tau_0/\rho_o|^{1/2}$ and f^{-1} may be used to express (9) in
 866 dimensionless form:

$$\mathbf{k} \times \mathbf{U} = -\frac{d\tau}{dz}, \quad z < 0. \quad (\text{A6})$$

867 In (A6), the dimensional velocity, stress, and depth have been scaled by u_* , $\rho_0 u_*^2$, and $D_o = u_*/f$,
 868 respectively. The corresponding dimensionless boundary conditions are:

$$\mathbf{U} \rightarrow 0 \quad \text{as} \quad z \rightarrow -\infty, \quad (\text{A7})$$

$$\mathbf{U} - \mathbf{V}/\alpha = -(\mathbf{U}_G - \mathbf{V}_G/\alpha) \quad \text{at} \quad z = 0, \quad (\text{A8})$$

$$\tau = 1 \quad \text{at} \quad z = 0, \quad (\text{A9})$$

869 where

$$\alpha = \frac{u_*}{v_*} = \left(\frac{\rho_a}{\rho_o} \right)^{1/2} \approx 0.035 \quad (\text{A10})$$

870 is the ratio of u_* to the atmospheric friction velocity $v_* = |\tau_0/\rho_a|^{1/2}$ and the ocean and atmospheric
 871 velocities have been scaled by u_* and v_* respectively.

872 The dimensionless problem for the coupled boundary layers, consisting of (A6) and (A7)-(A10)
 873 supplemented by the atmospheric equivalents of (A6) and (A7), would have a universal structure
 874 if there were no additional relevant length scales. Samelson (2020) has shown that for coupled
 875 boundary layers with this universality, the drift velocity \mathbf{U}_0 at the interface is the α -weighted
 876 average of the free-stream velocities, which for the rotating system is

$$\mathbf{U}_0 = \frac{\mathbf{U}_G + \alpha \mathbf{V}_G}{1 + \alpha}. \quad (\text{A11})$$

877 For the ocean-atmosphere case, this prediction would be consistent with the classical rule-of-thumb
 878 for surface drift, according to which \mathbf{U}_0 is directed 15° to the right of the wind (in the Northern
 879 Hemisphere) at 3% of the wind speed. However, there is in this case at least one another relevant
 880 length scale, associated with the presence of gravity waves at the air-sea interface. For example,
 881 Charnock length scales $l_{Co*} = u_*^2/g$ for the ocean and $l_{Ca*} = v_*^2/g$ for the atmosphere can be defined,
 882 where g is the acceleration of gravity. The corresponding dimensionless length scales $l_{Co} = u_* f/g$

883 and $l_{Ca} = v_* f / g$ differ by a factor of α , suggesting the possibility of departures from the universal,
884 antisymmetric structure.

885 Consistent with general experience, the estimate (A11) indicates that under most conditions the
886 dimensional $|U_0| \ll V_{10}$, where V_{10} is the 10-m wind speed, so that to first order the stress τ_0
887 is independent of the surface drift. This motivates the traditional neglect of the third boundary
888 condition (A3) or (A8), the continuity of the velocity at the air-sea interface, in the specification
889 of the ocean boundary layer problem. Note, however, that ocean surface velocities can be detected
890 in observational estimates of the dependence of air-sea momentum flux on the 10-m wind, as the
891 scatter in the observed statistical relationship is measurably reduced when the relative wind – the
892 difference between the 10-m wind and the ocean surface velocity – is used in place of the 10-m wind
893 (Edson et al. 2013). In the observational estimates, this ocean surface velocity is generally taken
894 as the velocity near 10-m depth (Bigorre et al. 2013), the shallowest depth at which reliable ocean
895 current measurements are typically available. It thus may differ significantly from the interface
896 velocity U_0 , suggesting that a correction to the observed drag coefficient would be necessary if
897 the relative wind were instead computed with respect to the interface velocity, as would be most
898 appropriate theoretically.

899 **References**

- 900 Agrawal, Y., E. Terray, M. Donelan, P. Hwang, A. W. II, W. Drennan, K. Kahma, and S. Kitaig-
901 orodskii, 1992: Enhanced dissipation of kinetic energy beneath surface waves. *Nature*, **359**,
902 219–220.
- 903 Anis, A., and J. N. Moum, 1995: Surface wave-turbulence interactions: scaling $\varepsilon(z)$ near the sea
904 surface. *Journal of Physical Oceanography*, **25 (9)**, 2025 – 2045.
- 905 Ardhuin, F., Y. Aksenov, A. Benetazzo, L. Bertino, P. Brandt, and E. Caubet, 2017: Measuring
906 currents, ice drift, and waves from space: the Sea Surface KInematics Multiscale monitoring
907 (SKIM) concept. *Ocean Sci.*, **14**, 337–354.
- 908 Ardhuin, F., L. Marié, N. Rasclé, P. Forget, and A. Roland, 2009: Observation and estimation of
909 Lagrangian, Stokes, and Eulerian currents induced by wind and waves at the sea surface. *Journal*
910 *of Physical Oceanography*, **39 (11)**, 2820–2838.
- 911 Banner, M. L., and W. L. Peirson, 1998: Tangential stress beneath wind-driven air–water interfaces.
912 *Journal of Fluid Mechanics*, **364**, 115–145.
- 913 Batchelor, G. K., 1967: *An Introduction to Fluid Dynamics*. Cambridge University Press.
- 914 Bigorre, S. P., R. A. Weller, J. B. Edson, and J. D. Ware, 2013: A Surface Mooring for Air–
915 Sea Interaction Research in the Gulf Stream. Part II: Analysis of the Observations and Their
916 Accuracies. *Journal of Atmospheric and Oceanic Technology*, **30 (3)**, 450–469.
- 917 Blackadar, A. K., and H. Tennekes, 1968: Asymptotic similarity in neutral barotropic planetary
918 boundary layers. *J. Atmos. Sci.*, **25**, 1015–1020.
- 919 Bourassa, M. A., 2000: Shear stress model for the aqueous boundary layer near the air-sea interface.
920 *J. Geophys. Res.*, 1169–1176.
- 921 Breivik, Ø., J.-R. Bidlot, and P. A. Janssen, 2016: A Stokes drift approximation based on the
922 Phillips spectrum. *Ocean Modelling*, **100**, 49 – 56.
- 923 Bye, J. A. T., 1988: The coupling of wave drift and wind velocity profiles. *J. Mar. Res.*, **46 (3)**,
924 457–472.

- 925 Callies, U., N. Groll, J. Horstmann, H. Kapitza, H. Klein, S. Maßmann, and F. Schwichtenberg,
926 2017: Surface drifters in the German Bight: model validation considering windage and Stokes
927 drift. *Ocean Science*, **13 (5)**, 799–827.
- 928 Churchill, J. H., and G. T. Csanady, 1983: Near-surface measurements of quasi-lagrangian veloci-
929 ties in open water. *Journal of Physical Oceanography*, **13 (9)**, 1669 – 1680.
- 930 Craig, P. D., and M. L. Banner, 1994: Modeling wave-enhanced turbulence in the ocean surface
931 layer. *J. Phys. Oceanogr.*, **24**, 2546–2559.
- 932 Edson, J. B., and Coauthors, 2013: On the exchange of momentum over the open ocean. *J. Phys.*
933 *Oceanogr.*, **43**, 1589–1610.
- 934 Ekman, V. W., 1905: On the influence of the Earth’s rotation on ocean currents. *Arkiv Mat.*
935 *Astronom. Fyzik*, **2**, 1–53.
- 936 Ellison, T. H., 1956: Atmospheric turbulence. *Surveys in Mechanics*, G. K. Batchelor, and R. M.
937 Davies, Eds., Cambridge University Press, 400–430.
- 938 Garratt, J. R., 1992: *The atmospheric boundary layer*. Cambridge University Press.
- 939 Grare, L., L. Lenain, and W. K. Melville, 2018: Vertical profiles of the wave-induced airflow above
940 ocean surface waves. *Journal of Physical Oceanography*, **48 (12)**, 2901–2922.
- 941 Grare, L., N. M. Statom, N. Pizzo, and L. Lenain, 2021: Instrumented Wave Gliders for air-sea
942 interaction and upper ocean research. *Frontiers in Marine Science*, **8**, 888.
- 943 Greenan, B. J. W., N. S. Oakey, and F. W. Dobson, 2001: Estimates of dissipation in the ocean
944 mixed layer using a quasi-horizontal microstructure profiler. *Journal of Physical Oceanography*,
945 **31 (4)**, 992 – 1004.
- 946 Hasselmann, K., 1970: Wave-driven inertial oscillations. *Geophysical Fluid Dynamics*, **1 (3-4)**,
947 463–502.
- 948 Hughes, K. G., J. N. Moum, and E. L. Shroyer, 2020: Evolution of the velocity structure in the
949 diurnal warm layer. *Journal of Physical Oceanography*, **50 (3)**, 615 – 631.
- 950 Jenkins, A. D., 1989: The use of a wave prediction model for driving a near-surface current model.
951 *Dt. hydrogr. Z.*, **42**, 133–149.

- 952 Keulegan, G. H., 1951: Wind tides in small closed channels. *J. Res. Natl. Bur. Stnds.*, **46**, 358–391.
- 953 Kudryavtsev, V., V. Shrira, V. Dulov, and V. Malinovsky, 2008: On the vertical structure of
954 wind-driven sea currents. *J. Phys. Oceanogr.*, **38**, 2121–2144.
- 955 Large, W. G., J. C. McWilliams, and S. C. Doney, 1994: Oceanic vertical mixing: a review and
956 a model with a nonlocal boundary layer parameterization. *Oceanographic Literature Review*, **7**,
957 527.
- 958 Laxague, N. J. M., and C. J. Zappa, 2020: Observations of mean and wave orbital flows in the
959 ocean’s upper centimetres. *Journal of Fluid Mechanics*, **887**, A10.
- 960 Lenain, L., and N. Pizzo, 2021: Modulation of surface gravity waves by internal waves. *Journal*
961 *of Physical Oceanography*, **51 (9)**, 2735 – 2748.
- 962 Lewis, D. M., and S. E. Belcher, 2004: Time-dependent, coupled, Ekman boundary layer solutions
963 incorporating Stokes drift. *Dynamics of Atmospheres and Oceans*, **37**, 313–351.
- 964 Lund, B., and Coauthors, 2018: Near-surface current mapping by shipboard marine X-band radar:
965 A validation. *Journal of Atmospheric and Oceanic Technology*, **35 (5)**, 1077 – 1090.
- 966 Madsen, O. S., 1977: A realistic model of the wind-induced Ekman boundary layer. *Journal of*
967 *Physical Oceanography*, **7 (2)**, 248–255.
- 968 McWilliams, J. C., and J. M. Restrepo, 1999: The wave-driven ocean circulation. *Journal of*
969 *Physical Oceanography*, **29 (10)**, 2523 – 2540.
- 970 McWilliams, J. C., P. Sullivan, and C.-H. Moeng, 1997: Langmuir turbulence in the ocean. *J.*
971 *Fluid Mech.*, **334 (1–30)**.
- 972 Mellor, G., 2016: On theories dealing with the interaction of surface waves and ocean circulation.
973 *J. Geophys. Res.*, **121 (4474–4486)**.
- 974 Melville, W. K., 1996: The role of surface-wave breaking in air-sea interaction. *Annual Review of*
975 *Fluid Mechanics*, **28 (1)**, 279–321.
- 976 Miles, J. W., 1957: On the generation of surface waves by shear flows. *J. Fluid Mech.*, **3**, 185–204.

- 977 Morey, S. L., N. Wienders, D. S. Dukhovskoy, and M. A. Bourassa, 2018: Measurement charac-
978 teristics of near-surface currents from ultra-thin drifters, drogued drifters, and HF radar. *Remote*
979 *Sensing*, **10** (10), 1633.
- 980 Phillips, O. M., 1957: On the generation of waves by turbulent wind. *J. Fluid Mech.*, **2**, 417–445.
- 981 Phillips, O. M., 1977: *The dynamics of the upper ocean*. 2nd ed., Cambridge University Press.
- 982 Pizzo, N., W. K. Melville, and L. Deike, 2019: Lagrangian transport by nonbreaking and breaking
983 deep-water waves at the ocean surface. *Journal of Physical Oceanography*, **49** (4), 983–992.
- 984 Pizzo, N. E., L. Deike, and W. K. Melville, 2016: Current generation by deep-water breaking
985 waves. *Journal of Fluid Mechanics*, **803**, 275–291.
- 986 Pollard, R., 1973: Interpretation of near-surface current meter observations. *Deep Sea Research*
987 *and Oceanographic Abstracts*, **20** (3), 261 – 268.
- 988 Pollard, R. T., 1970: Surface waves with rotation: An exact solution. *Journal of Geophysical*
989 *Research (1896-1977)*, **75** (30), 5895–5898.
- 990 Rapp, R. J., and W. K. Melville, 1990: Laboratory measurements of deep-water breaking waves.
991 *Philosophical Transactions of the Royal Society of London. Series A, Mathematical and Physical*
992 *Sciences*, **331** (1622), 735–800.
- 993 Rascle, N., and F. Ardhuin, 2009: Drift and mixing under the ocean surface revisited: Stratified
994 conditions and model-data comparisons. *Journal of Geophysical Research: Oceans*, **114** (C2).
- 995 Resio, D. T., V. R. Swail, R. E. Jensen, and V. J. Cardone, 1999: Wind speed scaling in fully
996 developed seas. *Journal of Physical Oceanography*, **29** (8), 1801 – 1811.
- 997 Rodriguez, E., M. Bourassa, D. Chelton, J. T. Farrar, D. Long, D. Perkovic-Martin, and R. Samel-
998 son, 2019: The Winds and Currents Mission concept. *Front. Mar. Sci.* **6**, **438**.
- 999 Rodriguez, E., A. Wineteer, D. Perkovic-Martin, T. Gal, B. Stiles, N. Niamsuwan, and R. Monje,
1000 2018: Estimating ocean vector winds and currents using a Ka-band pencil-beam Doppler
1001 scatterometer. *Remote Sensing*, **10**, 576.
- 1002 Samelson, R. M., 2020: Turbulent universality and the drift velocity at the interface between two
1003 homogeneous fluids. *Physics of Fluids*, **32** (8), 082 107.

- 1004 Samelson, R. M., L. W. O’Neill, D. B. Chelton, E. D. Skillingstad, P. L. Barbour, and S. M. Durski,
1005 2020: Surface stress and atmospheric boundary layer response to mesoscale SST structure
1006 in coupled simulations of the northern California Current System. *Monthly Weather Review*,
1007 **148 (1)**, 259–287.
- 1008 Samelson, R. M., E. D. Skillingstad, S. M. Durski, and P. L. Barbour, 2021: Surface currents and
1009 relative-wind stress in coupled ocean-atmosphere simulations of the northern California Current
1010 System. *in preparation*.
- 1011 Santala, M. J., and E. A. Terray, 1992: A technique for making unbiased estimates of current shear
1012 from a wave-follower. *Deep-Sea Research I*, **39**, 607–622.
- 1013 Skillingstad, E. D., J. Duncombe, and R. M. Samelson, 2017: Baroclinic frontal instabilities and
1014 turbulent mixing in the surface boundary layer. Part ii: Forced simulations. *Journal of Physical
1015 Oceanography*, **47 (10)**, 2429–2454.
- 1016 Smit, P. B., T. T. Janssen, and T. H. C. Herbers, 2017: Nonlinear wave kinematics near the ocean
1017 surface. *Journal of Physical Oceanography*, **47 (7)**, 1657–1673.
- 1018 Spivak, M., 1965: *Calculus on Manifolds*. Benjamin, New York, 146 pp.
- 1019 Stokes, G. G., 1847: On the theory of oscillatory waves. *Trans. Camb. Phil. Soc.*, **8**, 441–455.
- 1020 Sullivan, P. P., and J. C. McWilliams, 2010: Dynamics of winds and currents coupled to surface
1021 waves. *Annual Review of Fluid Mechanics*, **42 (1)**, 19–42.
- 1022 Sutherland, P., and W. K. Melville, 2015: Field measurements of surface and near-surface tur-
1023 bulence in the presence of breaking waves. *Journal of Physical Oceanography*, **45 (4)**, 943 –
1024 965.
- 1025 Suzuki, N., and B. Fox-Kemper, 2016: Understanding Stokes forces in the wave-averaged equations.
1026 *Journal of Geophysical Research: Oceans*, **121 (5)**, 3579–3596.
- 1027 Taylor, G. I., 1915: Eddy motion in the atmosphere. *Phil. Trans. A*, **215**, 1–26.
- 1028 Thomson, J., 2012: Wave breaking dissipation observed with “SWIFT” drifters. *Journal of Atmo-
1029 spheric and Oceanic Technology*, **29 (12)**, 1866 – 1882.

- 1030 Thomson, J., M. S. Schwendeman, S. F. Zippel, S. Moghimi, J. Gemmrich, and W. E. Rogers,
1031 2016: Wave-breaking turbulence in the ocean surface layer. *Journal of Physical Oceanography*,
1032 **46 (6)**, 1857 – 1870.
- 1033 Troen, I., and L. Mahrt, 1986: A simple model of the atmospheric boundary layer sensitivity to
1034 surface evaporation. *Bound.-Layer Meteor.*, **37**, 129–148.
- 1035 Ursell, F., 1950: On the theoretical form of ocean swell on a rotating Earth. *Geophysical Journal*
1036 *International*, **6 (s1)**, 1–8.
- 1037 Van Dorn, W. G., 1953: Wind stress on an artificial pond. *J. Mar. Res.*, **12**, 249–276.
- 1038 Weber, J. E., 1983: Steady wind- and wave-induced currents in the open ocean. *Journal of Physical*
1039 *Oceanography*, **13 (3)**, 524–530.
- 1040 Weber, J. E., 1981: Ekman currents and mixing due to surface gravity waves. *Journal of Physical*
1041 *Oceanography*, **11 (10)**, 1431 – 1435.
- 1042 Xu, Z., and A. J. Bowen, 1994: Wave- and wind-driven flow in water of finite depth. *J. Phys.*
1043 *Oceanogr.*, **24**, 1850–1866.
- 1044 Zelenke, B., C. O’Connor, C. Barker, and C. Beegle-Krause, 2012: General NOAA Operational
1045 Modeling Environment (GNOME) technical documentation. Tech. Rep. Technical Memorandum
1046 NOS OR&R 41, National Oceanic and Atmospheric Administration, Office of Response and
1047 Restoration: Seattle, WA, USA.